

# The Nucleon Axial Form Factor from Averaging Lattice QCD Results

Aaron S. Meyer\*

*Nuclear and Chemical Sciences Division, Lawrence Livermore National Laboratory, Livermore, CA 94550, USA*

(Dated: January 7, 2026)

Flagship neutrino oscillation experiments depend on precise and accurate theoretical knowledge of neutrino-nucleon cross sections across a variety of energies and interaction mechanisms. Key ingredients to the amplitudes that make up these cross sections are parameterized form factors. The axial form factor describing a weak interaction with a nucleon is part of one of the primary neutrino-nucleon interaction mechanisms, quasielastic scattering, yet this form factor is uncertain and its precision is limited by the availability of data for a neutrino scattering with nucleons or small nuclear targets. Lattice Quantum Chromodynamics (LQCD) now offers another approach for obtaining mathematically rigorous constraints of the axial form factor from theoretical calculations with complete systematic error budgets. In this work, strategies for averaging LQCD results are explored, including both a random sampling of form factor values across momentum transfers as well as an averaging strategy based on analytic calculations of form factor derivatives. Fits to  $z$  expansion parameterizations are reported and compared against neutrino-hydrogen and neutrino-deuterium scattering data.

## I. INTRODUCTION

Experiments that measure neutrino scattering and interactions are evolving from an era of discovery to one of precision. Flagship neutrino oscillation experiments [1–5] are preparing for their initial data taking phases, where they will detect an unprecedented number of neutrino interactions. These measurements will help to close the gaps in scientific understanding of the parameters that govern neutrino flavor oscillation.

To help achieve and surpass the goals put forth by neutrino experiments, sufficient theoretical support must also be provided that can aid in interpretation of detected events. Neutrino beams contain a broad spectrum of neutrino energies, preventing accurate quantification of the neutrino energy on an event-by-event basis. Neutrino interactions must instead be described as statistical distributions and the corresponding neutrino energies reconstructed from those distributions. This process requires precise and accurate knowledge of neutrino cross sections across a range of neutrino energies and interaction topologies.

The cross sections describing neutrino interactions with nuclear matter are constructed from weak interaction amplitudes. Theoretical characterization of these amplitudes depend largely on free nucleon matrix elements, which have historically been obtained from scattering with small nuclear targets. Parameterized by form factors that depend upon the four-momentum transfer squared ( $Q^2$ ), the vector contributions to low-energy neutrino scattering with a nucleon target can be precisely obtained from electron-proton scattering data. The axial contributions, on the other hand, can only be obtained from measurements sensitive to weak matrix elements and therefore relatively low-statistics experiments. Measurements from bubble chambers containing deuterium

fills [6–14] have been the most constraining on the primary source of uncertainty for neutrino cross section, the axial form factor. Other works using pion electroproduction [15–17] and muon capture [18–21] are also sensitive to the axial form factor. More recently, a result for the axial form factor obtained from antineutrino-hydrogen scattering has also been published [22, 23].

Due to advances in computational techniques and the growth of computing power with Moore’s Law, theoretical computations of weak matrix elements with neutrinos are now possible using Lattice Quantum Chromodynamics (LQCD). LQCD calculations access the properties of hadrons by means of numerical evaluations of the path integral formulation, providing mathematically rigorous predictions and systematically improvable uncertainties on hadronic quantities such as masses and matrix elements. Though experiments face difficulties measuring neutrino scattering with free nucleon targets, calculating the axial matrix elements with LQCD is straightforward. This makes the use of LQCD an appealing candidate as a source of constraint for neutrino cross sections.

Historically, LQCD calculations have had difficulty reproducing the axial coupling,  $g_A$ . This value is precisely known from neutron beta decay measurements [24] and therefore a benchmark quantity for LQCD calculations with nucleon states. Past LQCD calculations underpredicted  $g_A$  by as much as 20% [25]. This was later attributed to poorly-constrained pion-nucleon excited state contributions that were enhanced by the axial current [26–36]. With a better understanding of the relevant contamination, LQCD calculations of the axial coupling are now able to reproduce the experimental value to within 1% [37–42].

With relevant expertise and demonstrable control of the axial coupling, LQCD collaborations have started reporting calculations of the axial form factor  $Q^2$  dependence. Several collaborations have released results within the past half decade using a nontrivial variety of quark actions and analysis techniques. These calcu-

\* [asmeyer.physics@gmail.com](mailto:asmeyer.physics@gmail.com); [meyer54@llnl.gov](mailto:meyer54@llnl.gov)

lations all pass internal consistency checks of the axial form factor against the pseudoscalar and induced pseudoscalar form factors by making use of the generalized Goldberger-Treiman relation and pion pole dominance ansatz [32, 33, 36, 43, 44]. The collaborations also agree well with each other, providing a consistent narrative from the LQCD community.

Surprisingly, the axial form factor predictions obtained from LQCD calculations exhibit a significant tension at high  $Q^2$  compared to the axial form factor constraints originating from deuterium bubble chamber experiments [45–47]. These changes suggest that the quasielastic cross section should be enhanced by as much as 30% over the previous deuterium prediction, well outside of the 10% uncertainty. Within the same timeframe that the LQCD results appeared, accompanying evidence corroborating the need for an enhanced quasielastic cross section came in the form of Monte Carlo tunes to neutrino-nucleus data [48, 49] as well as a recent measurement of antineutrino-proton scattering [22, 23].

With several independent LQCD results already available, one might wonder how much the constraints on the axial form factor can be improved by averaging these results. This work provides such a prediction of the axial form factor by combining calculations from five different collaborations over four unique sets of gauge ensembles. These calculations provide nontrivial checks of consistency among each other and should be viewed as independent results. Attention is paid to the correlations between results that make use of the same gauge ensembles. This work was prepared in conjunction with a sister paper [50], where many details about the experimental connections can be found.

This document is organized as follows. Sec. II discusses details associated with parameterizing the form factors, the construction of a sufficient set of fit residuals, and how to handle correlations between LQCD results. Sec. III gives the details of the LQCD results that were used in this work and lists the parameters of the form factors that go into the average. Sec. IV gives details about the fits, tests of systematics effects, and consistency checks between different fit methods. Several parameterizations of the form factor under different assumptions are reported. Some concluding remarks are given in Sec. V.

## II. FIT DETAILS

This section describes the details of how the fits to LQCD results are carried out. Sec. II A enumerates the relevant parameterizations that appear in the literature and in this work. Sec. II B gives details on how fits are constructed, including the residuals that are optimized over and the assumed covariances on these residuals. Sec. II C describes strategies for addressing unknown correlations in the LQCD parameterizations due to shared gauge ensembles.

### A. Form Factor Parameterizations

Historically, several parameterizations have been used to describe the shape and magnitude of the form factor. Although this work primarily focuses on the  $z$  expansion parameterization of Sec. II A 2, the dipole parameterization in Sec. II A 1 is also explored due to its widespread use.

#### 1. Dipole Parameterization

The historical choice of parameterization used for fitting the axial form factor has been the dipole parameterization [51], given by

$$F_A(Q^2) = g_A [1 + Q^2/M_A^2]^{-2}. \quad (1)$$

This parameterization has two free parameters:  $g_A$ , the axial coupling, which is fixed by precise neutron beta decay experiments; and  $M_A$ , also known as the axial mass parameter. The dipole form factor is also the Fourier transform of a simple exponentially decaying function in three dimensions.

One of the reasons this form factor has persisted for so long is that this parameterization has an asymptotic falloff proportional to  $Q^{-4}$  as  $Q^2 \rightarrow \infty$ , in agreement with the expectations from perturbative QCD [52]. However, this limiting behavior only becomes relevant for  $Q^2$  well outside of the range probed by neutrino experiments. Even if the form factor has the correct power-law falloff in the large  $Q^2$  limit, there is no guarantee that the prefactor multiplying that asymptotic falloff is correct.

The dipole parameterization of the axial form factor is overconstrained by neutrino scattering data. Given the precise constraints on  $g_A$ , the axial form factor has effectively one free parameter to constrain with neutrino scattering data. Different  $Q^2$  ranges result in different best-fit values for  $M_A$ , and fits to the full range typically result in poor fit quality and underestimated uncertainties. This resulted in an “axial mass problem,” where values of  $M_A$  reported by different sources disagreed by more than their quoted uncertainties.

To capture a more realistic range of uncertainties for the form factor,  $M_A$  has historically been considered with an inflated 10% relative uncertainty. This choice still assumes 100% correlation between different values of  $Q^2$ , providing no flexibility in the overall shape. More well-motivated choices with alternative parameterizations, for example the  $z$  expansion, result in more realistic uncertainties that are an order of magnitude larger than those of the dipole prediction. At least part of this larger uncertainty comes from allowing more flexibility in the form factor shape across  $Q^2$ .

## 2. *z* Expansion Parameterization

The *z* expansion parameterization [53, 54] is a conformal mapping that takes  $Q^2$  to a small expansion parameter *z* for the entire kinematic range probed by quasielastic scattering. The definition of the conformal mapping is

$$z = \frac{\sqrt{t_c + Q^2} - \sqrt{t_c - t_0}}{\sqrt{t_c + Q^2} + \sqrt{t_c - t_0}}. \quad (2)$$

With this conformal mapping, the form factor can be written as a power series in *z*,

$$F_A(z) = \sum_{k=0}^{\infty} a_k z^k. \quad (3)$$

In practice, the sum is taken up to some finite order  $k_{\max}$  that is determined by the fit range and fidelity of the data. The parameter  $t_c$  is bounded by the particle production threshold for the axial current interaction, at  $t_c \leq (3M_\pi)^2$ . The last remaining parameter,  $t_0$ , fixes the value of  $Q^2$  for which  $z(Q^2 = -t_0) = 0$  is satisfied. The value of  $t_0$  can be chosen for convenience and typically is chosen to minimize the maximum value of *z* over the entire kinematic range of interest.

The shape of the form factor can additionally be constrained with sum rules that enforce desirable behavior in the asymptotic  $Q^2 \rightarrow \infty$  limit. These sum rules are obtained by solving for derivatives of the form factor with respect to *z* taken as  $z \rightarrow 1$  ( $Q^2 \rightarrow \infty$ ),

$$\sum_{k=n}^{k_{\max}} k(k-1)\dots(k-n+1)a_k = 0, n \in \{0, 1, 2, 3\}. \quad (4)$$

These sum rules enforce the conditions

$$\lim_{Q^2 \rightarrow \infty} \left[ \frac{\partial}{\partial Q^2} \right]^n F_A(Q^2) = 0. \quad (5)$$

Given the coefficients  $a_k$  up to order  $k_{\max} - 4$ , the sum rules provide an exact relation to solve for the last 4 remaining coefficients. Imposing sum rules as a constraint during fits to the *z* expansion does not significantly affect the fit results, typically resulting in a smaller uncertainty for the high- $Q^2$  range beyond the data and central values shifted within the  $1\sigma$  uncertainty band.

The constraints on  $g_A$  from neutrino scattering and from LQCD are not competitive with constraints from neutron beta decay measurements. Instead of treating the value of  $g_A$  as a fit parameter, an additional constraint is imposed to fix the intercept

$$F_A(Q^2 = 0) = g_A^\beta. \quad (6)$$

This constraint is enforced by fixing  $a_0$  to reproduce  $g_A^\beta = 1.2754$ , taken from PDG [24]. A summary of the full set of parameters adopted in this work is given in Table I.

Parameter	Value
$g_A^\beta$ [24]	1.2754
$t_c$	$9 \cdot (0.134 \text{ GeV})^2$
$t_0$	$-0.50 \text{ GeV}^2$
# sum rules	4

TABLE I. A list of fixed parameters needed to fit the axial form factor in this work. The first column gives the fit parameter, and the second column gives the value that was used for that parameter in this work.

## B. Fit Methods

A set of residuals must be defined in order to construct a  $\chi^2$  loss function to optimize. There is more than one way to build a set of residuals and so various choices must be considered in order to ensure that the fits are not sensitive to the particular choices that were used. Once a meaningful set of residuals  $r_i$  has been decided upon, the loss function

$$\chi^2 = \sum_{ij} r_i(\mathbf{a}) \left[ C_{ij}^{\mathbf{r}} \right]^{-1} r_j(\mathbf{a}) \quad (7)$$

can be minimized to find a set of best-fit parameters. In this case, the parameters  $\mathbf{a}$  to minimize are exactly the *z* expansion coefficients  $a_k$  in Eq. (3). For constructing a covariance of the residuals, it is simple to use Gaussian error propagation to define a residual covariance

$$C_{ij}^{\mathbf{r}} = \sum_{kl} [\nabla_{\alpha_k} r_i] C_{kl}^{\boldsymbol{\alpha}} [\nabla_{\alpha_l} r_j] \quad (8)$$

using the covariance  $C^{\boldsymbol{\alpha}}$  over the input parameters  $\alpha_k$ .

Two fit methods, leading to different residuals, will be employed in this work. Sec. II B 1 describes a fit using the central values and derivatives of the form factor at specific values of  $Q^2$ . As an alternative, Sec. II B 2 considers fits where the full  $Q^2$  range of the form factor is stochastically sampled and fit.

### 1. Fit to Derivatives

The axial form factor parameterizations from LQCD results can be combined analytically by fitting to the form factor central value and its derivatives at fixed values of  $Q^2$ ,

$$\left[ \frac{\partial}{\partial Q^2} \right]^n F_A(Q^2), n \geq 0. \quad (9)$$

With this choice, the set of residuals then becomes

$$r_i = \left[ \frac{\partial}{\partial Q^2} \right]^{n_i} \left[ F_A(Q^2; \boldsymbol{\alpha}_{(i)}) - F_A(Q^2; \mathbf{a}) \right] \Big|_{Q^2=Q_i^2} \quad (10)$$

for choices of derivative order  $n_i$ ,  $Q^2$  evaluation point  $Q_i^2$ , and an input parameterization with coefficients  $\boldsymbol{\alpha}_{(i)}$ .

The evaluation point  $Q^2 = -t_0$  is particularly convenient for the  $z$  expansion parameterization because this choice yields the relations

$$F_A(Q^2 = -t_0) = a_0, \\ \frac{\partial}{\partial Q^2} F_A \Big|_{Q^2 = -t_0} = a_1 \frac{\partial z}{\partial Q^2}. \quad (11)$$

All terms proportional to a power of  $z$  vanish due to the requirement that  $z(Q^2 = -t_0) = 0$ . Higher-order derivatives of the form factor yield linear combinations of the  $a_k$  multiplying derivatives of  $z$ , such as

$$\left[ \frac{\partial}{\partial Q^2} \right]^2 F_A \Big|_{Q^2 = -t_0} = 2a_2 \left[ \frac{\partial z}{\partial Q^2} \right]^2 + a_1 \left[ \frac{\partial}{\partial Q^2} \right]^2 z. \quad (12)$$

Although the nominal choice will be to compute the form factor and its derivatives at  $Q^2 = -t_0$ , other choices will be explored in this work.

There are several advantages to fitting derivatives of the form factor. Although this fit procedure is formulated in a way that is convenient for comparing  $z$  expansion parameterizations, the dependence only on form factor derivatives with respect to  $Q^2$  means the procedure can be applied to any parameterization. The  $z$  expansion also exhibits linear behavior over a large range of parameter values, meaning that most of the form factor shape is captured in these first two derivatives even when they are computed only at a single value of  $Q^2$ . Since most LQCD parameterizations do not constrain more than 3 parameters, the assumption is that the last parameter is absorbing contributions from other higher-order terms as well, and therefore derivatives beyond first order are not expected to be well constrained. These effects are expected to be primarily absorbed by the coefficients relegated to the sum rules, with only small effects seen in the lower order fit coefficients. Another advantage of this formulation is that the form factor derivatives and uncertainty propagation can be computed analytically provided that the number of residuals for any  $z$  expansion parameterization does not exceed the number of  $z$  expansion coefficients. The bulk of the form factor shape can therefore be extracted from just a few residuals with this well-defined fit procedure.

There are also disadvantages to fitting form factor derivatives as recommended in this section. There is ambiguity in how to select the best momentum transfer value (or values) at which to evaluate the form factors, leading to a potential for bias. For this, there at least exists the natural expansion point at  $Q^2 = -t_0$  that leads to Eq. (11), providing some measure of guidance. As another drawback, care must be taken to avoid constructing sets of residuals that are not linearly independent, which can lead to an uninvertible covariance matrix. This can be especially troublesome in nontrivial circumstances, for instance if all of the results are evaluated at the same  $Q^2$ , or if derivatives are always evaluated at  $Q^2 = -t_0$  and the order of the expansion is greater than the number of

included derivatives. In such circumstances, one can run into uninvertible covariance matrices even for  $k_{\max}$  less than the number of degrees of freedom. These deficiencies will be explored in the tests in Sec. IV A.

In general,  $g_A$  is an output of LQCD calculations rather than an input. For this reason, the constraint on  $g_A$  in Eq. (6) is not typically employed in the reported LQCD results, instead only taking their own constraint on  $g_A$  to fix the form factor intercept. To match onto the results from neutrino scattering in a sister paper [50], the constraint of Eq. (6) will be used when fitting LQCD results here. This introduces a complication. Some LQCD results use  $t_0 = 0$  for simplicity, meaning that the matching condition in Eq. (11) should be performed at  $Q^2$  where the form factor is not allowed to vary. As a consequence, the residual for the form factor central value computed at  $Q^2 = 0$  will be independent of all fit parameters. Since higher-order  $Q^2$  derivatives are independent of the  $z$  expansion coefficient  $a_0$ , matching the fits at  $Q^2 = 0$  then potentially drops the most strongly constrained  $z$  expansion coefficient from these parameterizations. The resolution is simple: instead of computing the form factor and its derivatives at  $Q^2 = 0$ , the form factor matching is instead performed at some finite nonzero  $Q^2$ . This evaluation point will be varied and selected to maximize the uncertainty across  $Q^2$ .

## 2. Fit to Sampled Form Factor

A more straightforward way to fit the form factor is to sample the form factor central values over a fixed set of  $Q^2$  points. The residuals are then simply

$$r_i = \left[ F_A(Q^2; \boldsymbol{\alpha}_{(i)}) - F_A(Q^2; \boldsymbol{a}) \right] \Big|_{Q^2 = Q_i^2}, \quad (13)$$

defined with sampled  $Q^2$  values  $Q_i^2$  and input parameters  $\alpha_i$  like in Eq. (10). The typical strategy is to choose a set of fixed, evenly-spaced set of  $Q^2$  points and use the same  $Q^2$  values for all parameterizations that are being averaged.

Rather than rely on Gaussian uncertainty propagation, random values of the form factor parameters are selected respecting the covariances between the parameters. The covariances are used to generate a set of stochastically sampled form factor curves over the full range of  $Q^2$  using each parameterization. For each of these samples, the form factor is fit and the stochastic samples of the results are used to generate a covariance on the final fit parameters. The residuals in Eq. (13) are assumed to be uncorrelated to avoid the problem of an uninvertible covariance matrix, since the number of  $Q^2$  values exceeds the number of input LQCD parameters.

### 3. Translated $z$ expansion

The observation of Eq. (11) hints at a scheme for comparing  $z$  expansion parameterizations that have been generated with different choices of  $t_c$ ,  $t_0$ , and  $k_{\max}$ . Given a set of  $z$  expansion coefficients for one parameterization, another parameterization can be obtained by computing derivatives with respect to  $z$ ,

$$a_k = \frac{1}{k!} \left. \frac{d^k F_A(z)}{dz^k} \right|_{z=0}. \quad (14)$$

To compute these derivatives, chain rule is applied to convert  $z$  derivatives to derivatives with respect to  $Q^2$ ,

$$\frac{d}{dz} \rightarrow \frac{dQ^2}{dz} \frac{d}{dQ^2}. \quad (15)$$

Both sets of derivatives, namely the derivatives of  $Q^2$  with respect to  $z$  and the derivatives of the form factor with respect to  $Q^2$ , can be computed analytically for  $z$  expansion parameterizations. The form factor derivatives with respect to  $Q^2$  are computed at the point  $Q^2 = -t_0$  for  $t_0$  defined in the new  $z$  expansion parameterization definition. This provides a simple to execute and well-defined procedure for converting  $z$  expansion results from one set of coefficients to another, allowing for direct comparison of  $z$  expansion coefficients even for independently defined parameterizations.

### C. Unknown Covariances

One challenge of combining LQCD results is the presence of hidden correlations due to the reuse of gauge configurations and unreported fit covariances. More than one procedure can be used to estimate the effects of such correlations, but these choices will only estimate the effects rather than definitively determine the contributions from correlations. This subsection describes the methods used to estimate the effects of unknown correlations. Sec. II C 1 applies a technique called covariance derating to probe the full space of available covariances to construct an upper-bound. As a comparison point, an alternative approach using the Schmelling procedure is detailed in Sec. II C 2. This choice is akin to what is used by the Flavor Lattice Averaging Group (FLAG) in other works involving LQCD results [55].

#### 1. Covariance Derating

One method for addressing missing covariances is to use covariance derating [56], which is particularly useful for the fit to form factor derivatives in Sec. II B 1. This method starts from a “naive” covariance where all unknown correlations are set to 0. After obtaining a best-fit result, all possible variations of the covariance matrix are tested up to a specified confidence level. This

yields a derating factor, which is multiplied into the covariance matrix to inflate the parameter uncertainties enough to cover the full range of possible variations. For testing goodness-of-fit, another derating factor may be obtained that scales down the  $\chi^2$  in a  $p$  value computation. The full functionality of the derating is available in the `nustattools` [57] package.

Some detail is required on the inputs to the derating algorithm. The derating algorithm takes the naive covariance  $C^\alpha$  of the input parameters  $\alpha$ , the optimized fit parameters  $a$ , and the Jacobian matrix  $\bar{J}$  of the model prediction with respect to the best-fit parameters at the minimum,

$$\bar{J}_{ij} = \frac{\partial r_i(a; \alpha)}{\partial a_j}. \quad (16)$$

The naive covariance is defined for the  $z$  expansion coefficients from LQCD results in this work. However, the fit “data” are not the  $z$  expansion coefficients themselves, but instead the form factor central values and derivatives computed from these coefficients. A second Jacobian transformation brings the covariance over the  $z$  expansion coefficients to one over the form factor derivatives. The transformation is

$$C^{F_A} = J C^\alpha J^T, \\ J_{jk} = \frac{\partial r_j(a; \alpha)}{\partial a_k}. \quad (17)$$

The composed Jacobian transformation  $J^{-1} \bar{J}$  is supplied as an input into the algorithm when computing the derating factors.

The total number of fit parameters does not always match the number of fit derivatives assumed in these fits. This produces a rectangular Jacobian matrix in Eq. (17), which renders the composed Jacobian  $J^{-1} \bar{J}$  uninvertible. To circumvent this issue, dummy residuals  $\tilde{r}$  are added to the fit and new dummy parameters  $\tilde{a}$  are added to exactly reproduce those residuals. This procedure does not change the total  $\chi^2$  or the degree-of-freedom counting. However, the presence of the dummy parameter enlarges the covariance, allowing for exploration of additional freedom from marginalized parameter combinations and yielding an invertible composed Jacobian. In this work, the extra linear combinations are proportional to the LQCD coefficients, i.e.

$$\tilde{r}_i = \alpha_i - \tilde{a}_i, \quad (18)$$

choosing the  $\alpha_i$  to be the highest-order  $z$  expansion coefficients.

The derating factors  $\beta$  indicate how much inflation is needed to account for unknown data correlations. For assessing the uncertainties from fitting, a covariance derating factor  $\beta^{\text{cov}}$  is obtained for scaling the covariance, enlarging the uncertainty:

$$C^{\text{derated}} = \beta^{\text{cov}} C^{\text{fit}}. \quad (19)$$

For assessing goodness-of-fit (GoF), a separate derating factor is computed that scales the  $\chi^2$  from a fit with the naive covariance in a  $p$  value computation with  $\nu$  degrees of freedom (DoF):

$$p^{\text{derated}} = p(\chi^2 / \beta^{\text{GoF}}, \nu). \quad (20)$$

This derated  $p$  value then serves as an upper bound on the possible agreement between models, allowing for tests of incompatibility but not guaranteeing compatibility. In this work, both the derated  $p$  value and the  $p$  value obtained from a naive covariance matrix,

$$p^{\text{naive}} = p(\chi^2, \nu), \quad (21)$$

are reported. The  $p$  value computed from the naive covariance is not to be interpreted as a lower bound, instead only as an additional qualitative reference point.

## 2. Schmelling Procedure

An alternative approach for assessing missing covariances is the procedure outlined by Schmelling [58], a choice that is commonly employed in FLAG averages<sup>1</sup>. For this procedure, two sampled quantities  $x_i$  with unknown correlations are treated as fractionally correlated with a fraction  $f$  in the range  $[0, 1]$ , with a covariance matrix computed from the respective variances  $\sigma_i^2$  as

$$\begin{aligned} C(x_1, x_2; f) &= \begin{pmatrix} \sigma_1^2 & f\sigma_1\sigma_2 \\ f\sigma_1\sigma_2 & \sigma_2^2 \end{pmatrix} \\ &= \begin{pmatrix} \sigma_1 & 0 \\ 0 & \sigma_2 \end{pmatrix} \begin{pmatrix} 1 & f \\ f & 1 \end{pmatrix} \begin{pmatrix} \sigma_1 & 0 \\ 0 & \sigma_2 \end{pmatrix}. \end{aligned} \quad (22)$$

The fraction  $f$  ideally would be adjusted to yield a reduced  $\chi^2$  of 1.

In LQCD results, usually only the statistical uncertainty is correlated. When this is true, using the full uncertainty in the offdiagonal correlations is not necessary. The offdiagonal covariance can instead be modified to the value

$$\begin{aligned} f\text{Cov}[x_1, x_2] &= f\sigma_{1;2}\sigma_{2;1} \\ \sigma_{i;j} &= \sqrt{\sum_{\alpha} [\sigma_i^{\alpha}]^2} \end{aligned} \quad (23)$$

where the sum inside the square root runs over only uncertainties that are correlated between the two results. For this work, only the statistical uncertainty is assumed to be correlated between any two LQCD results. The only results in this work that exhibit these unknown correlations also separately report their statistical and systematic (or total) uncertainties, so no alternative procedures are considered.

<sup>1</sup> For more details, the reader is referred to Section 2.3 of Ref. [55].

## III. SUMMARY OF LQCD PARAMETERIZATIONS

LQCD results that will be included in fits are discussed in this section. In particular, only LQCD results that report complete error budgets, including chiral, continuum, and finite volume corrections, are subject to inclusion in the fits as part of this work. However, several other collaborations have previous or ongoing efforts to further understand the form factors with LQCD [59–75]. The parameterizations used by each collaboration are given in detail in Secs. III A–III E. The results that are used are compared in Sec. III F.

### A. RQCD 2020

The RQCD parameterization is defined as a  $k_{\text{max}} = 2$   $z$  expansion with no sum rule constraints imposed. The covariance for the RQCD result is not available in the literature. However, the supplemental material for Ref. [36] contains an array of means and errors for a large range of  $Q^2$  values. These values can be used to reverse engineer the parameterization and covariances used to generate those values good up to at least 4 significant digits. From this reverse engineering, the RQCD parameterization is found to be

$$(a_0, a_1, a_2) = (1.01333032, -1.71328189, -0.59048148) \quad (24)$$

with statistics-only covariance

$$\begin{pmatrix} 0.00055973 & -0.00192868 & 0.00075550 \\ -0.00192868 & 0.01415581 & -0.02897714 \\ 0.00075550 & -0.02897714 & 0.09590674 \end{pmatrix} \quad (25)$$

and a covariance for statistics and systematics together,

$$\begin{pmatrix} 0.00088551 & -0.00468337 & 0.01000718 \\ -0.00468337 & 0.08434121 & -0.16947322 \\ 0.01000718 & -0.16947322 & 0.35842788 \end{pmatrix}. \quad (26)$$

The reverse engineered parameterization yields the values  $t_c = 0.17150090 \text{ GeV}^2$  and  $t_0 = -0.17147395 \text{ GeV}^2$ .

### B. NME 2022

The NME parameterization is given as a  $z$  expansion parameterization up to  $k_{\text{max}} = 2$  with no sum rules imposed. The  $z$  expansion parameters are given in Eq. (56) of Ref. [76] as

$$(a_0, a_1, a_2) = (0.725(5), -1.63(3), -0.17(13)) \quad (27)$$

with  $t_c = (3 \cdot 0.135)^2 \text{ GeV}^2$  and  $t_0 = -0.50 \text{ GeV}^2$ . The covariance that accompanies these parameters is listed in

Eq. (I2) as

$$\begin{pmatrix} 2.188 \times 10^{-5} & -2.238 \times 10^{-5} & -1.155 \times 10^{-4} \\ -2.238 \times 10^{-5} & 8.549 \times 10^{-4} & 2.769 \times 10^{-3} \\ -1.155 \times 10^{-4} & 2.769 \times 10^{-3} & 1.811 \times 10^{-2} \end{pmatrix}. \quad (28)$$

Though NME tests the effects of systematic shifts due to the chiral, continuum, and finite volume extrapolations, the reported covariance does not include uncertainties for these variations. This leads to a form factor with precision below 1% for the entire  $Q^2$  range, below the uncertainty due to isospin-breaking corrections to the form factor [77]. NME notes that these extrapolations do not change the central value significantly and that allowing for these variations increases the uncertainty by about a factor of 3 [78].

To allow for uncertainty due to the extrapolation to the physical point, the NME covariance is scaled up by a factor of  $3^2 = 9$  or  $5^2 = 25$  for the purposes of this work. Even with the larger scale factor of 25, the NME result is the most precise and drives the uncertainty of the final average. Use of the smaller scale factor reduces the uncertainty by as much as 30% over the larger scale factor. For the remainder of this work, the larger scale factor of 25 is used to give a more conservative estimate and to allow the other LQCD results more contribution to the final average.

### C. Djukanovic *et al.* 2022

The Djukanovic *et al.* result [79] defines a  $k_{\max} = 2$  parameterization with  $t_c = (3 \cdot 0.135)^2 \text{ GeV}^2$  and  $t_0 = 0$ . The  $z$  expansion coefficients are

$$(a_0, a_1, a_2) = \begin{pmatrix} 1.225(39)(25), \\ -1.274(237)(70), \\ -0.379(592)(179) \end{pmatrix} \quad (29)$$

where the first uncertainty ( $\sigma_i^{\text{stat}}$ ) is statistical and the second ( $\sigma_i^{\text{syst}}$ ) is systematic. The total error is computed by summing the errors in quadrature,

$$\sigma_i^{\text{total}} = \sqrt{\sigma_i^{\text{stat}} + \sigma_i^{\text{syst}}}. \quad (30)$$

With the given correlation matrix

$$\rho = \begin{pmatrix} 1 & -0.67758 & 0.61681 \\ -0.67758 & 1 & -0.91219 \\ 0.61681 & -0.91219 & 1 \end{pmatrix}, \quad (31)$$

the covariance matrix is then computed from

$$\Sigma_{ij}^{\text{total}} = \sigma_i^{\text{total}} \rho_{ij} \sigma_j^{\text{total}}. \quad (32)$$

### D. ETM 2023

The ETM result [80] defines a  $k_{\max} = 3$  parameterization with  $t_c = (3 \cdot 0.135)^2 \text{ GeV}^2$  and  $t_0 = 0$ . The  $z$  expansion coefficients are

$$(a_0, a_1, a_2, a_3) = (1.245(28), -1.19(18), -0.54(61), -0.1(1.3)) \quad (33)$$

where the total uncertainty is given. The correlation matrix

$$\rho = \begin{pmatrix} 1 & -0.421 & 0.247 & -0.246 \\ -0.421 & 1 & -0.918 & 0.799 \\ 0.247 & -0.918 & 1 & -0.952 \\ -0.246 & 0.799 & -0.952 & 1 \end{pmatrix}, \quad (34)$$

is given, where the covariance matrix is computed with Eq. (32).

### E. PNDME 2023

The PNDME result [81] defines a  $k_{\max} = 2$  parameterization with  $t_c = (3 \cdot 0.140)^2 \text{ GeV}^2$  and  $t_0 = -0.25 \text{ GeV}^2$ . The  $z$  expansion coefficients are

$$(a_0, a_1, a_2) = (0.876(28), -1.669(99), 0.483(498)) \quad (35)$$

where the total uncertainty is given. The correlation matrix

$$\rho = \begin{pmatrix} 1 & -0.45170 & -0.02966 \\ -0.45170 & 1 & -0.24394 \\ -0.02966 & -0.24394 & 1 \end{pmatrix} \quad (36)$$

is given, where the covariance matrix is again computed with Eq. (32).

### F. LQCD Comparisons

The LQCD results obtained by different collaborations are nontrivial checks of consistency with each other. The strongest cross-validation of these results is the use of different quark actions, which are governed by different effective theories under an expansion in the lattice spacing. Strictly speaking, LQCD results with different actions cannot be compared with each other before taking the continuum limit, as they will have unknown corrections due to lattice spacing discretization errors. Additionally, results with different quark action necessarily use independently-generated gauge field configurations with different correlation functions. Results with nonoverlapping sets of gauge field configurations are therefore uncorrelated with each other by construction.

LQCD relies on computations across several ensembles of gauge configurations. These gauge configurations have

a variety of masses, lattice spacings, and volumes to control systematic effects from finite simulations. Physical mass ensembles are the gold standard, although they are more computationally costly than unphysical ensembles and have larger variances that lead to larger statistical uncertainties. Using unphysically heavy mass ensembles allows for more precise explorations of systematics due to lattice spacing and finite volume effects. The extrapolation to physical mass typically relies on Heavy Baryon Chiral Perturbation Theory [82, 83], which does not describe the extrapolation of baryon quantities to physical mass well [84, 85]. As a result, performing computations on one or more physical mass ensembles to anchor the extrapolation endpoint is desirable.

Each collaboration also has their own unique choice of fit methodology. After generating correlation functions as a function of Euclidean time, the correlation functions must be fit to extract the corresponding energies and matrix elements. The matrix elements are fit as a function of 4-momentum transfer  $Q^2$  to some fit parameterization, then the parameters of these form factors are extrapolated to the physical point at the chiral, continuum, and infinite-volume limits. These are the parameterizations reported as the form factors for QCD. The process for addressing these steps is not unique and different approaches confer different advantages and drawbacks.

Many collaborations fit to the known Euclidean time-dependence of the form factors using Bayesian priors, which can be written as (neglecting terms related to the finite volume):

$$\begin{aligned} C^{2pt}(t) &\approx \sum_{k=1}^{\infty} |z_k|^2 e^{-E_k t}, \\ C^{3pt}(t, \tau; \mathcal{J}) &\approx \sum_{k, \ell=1}^{\infty} z_k z_{\ell}^* \mathcal{J}_{k\ell} e^{-E'_k(t-\tau)} e^{-E_{\ell}\tau}. \end{aligned} \quad (37)$$

Here,  $C^{2pt}$  and  $C^{3pt}$  refer to the two-point and three-point functions, respectively. The two-point functions give access to overlap factors  $z_k$  and state energies  $E_k$ . The overlap factors connect the vacuum to states  $|k\rangle$  with the desired quantum numbers through an “interpolating operator”  $\mathcal{O}$ ,

$$z_k = \langle 0 | \mathcal{O} | k \rangle. \quad (38)$$

The index  $k$  connects to the ground state ( $k = 1$ ) as well as higher excited states ( $k \geq 2$ ), with  $k = 0$  being reserved for the vacuum. In practice, the number of excited states included in the fits is limited to a finite value. Contamination from improperly-constrained excited states is a concern in final results and typically part of the systematic error budget.

Given the overlap factors and energies computed with two-point functions, the three-point functions additionally give access to matrix elements of current  $\mathcal{J}$ ,

$$\mathcal{J}_{k\ell} = \langle k | \mathcal{J} | \ell \rangle. \quad (39)$$

To extract the axial matrix elements, the interpolating operator  $\mathcal{O}$  is typically a three-quark operator with some Fourier phase to impart a distinct 3-momentum, which couples strongly to a nucleon. The states  $|k\rangle$  that appear in Eqs. (38) and (39) would then be states with the same quantum numbers as the nucleon, including excitations such as nucleon-pion scattering states, and the current insertion  $\mathcal{J}$  could be defined as an axial current with fixed 3-momentum transfer  $\mathbf{q} = \mathbf{p}' - \mathbf{p}$ ,

$$\mathcal{J}_{k\ell} \rightarrow \langle N(\mathbf{p}') | \sum_{\mathbf{x}} \mathcal{A}(\mathbf{x}) e^{-i\mathbf{q} \cdot \mathbf{x}} | N(\mathbf{p}) \rangle. \quad (40)$$

As an alternative to fitting the correlation functions to the known forms in Eq. (37), RQCD uses a form that captures contributions from nucleon-pion excited states. In nucleon axial matrix elements, excited state terms with nucleon-pion states are typically difficult to constrain with two-point functions alone due to volume-suppressed overlap factors but are enhanced in three-point functions due to their coupling to amplitudes. The form used by RQCD adds terms with energies fixed to the values  $E, E' \rightarrow E_{\pi} + E_N$  and provides overlaps mimicking the kinematic dependence expected from chiral perturbation theory. This allows the fitter limited freedom with which to constrain nucleon-pion states without getting lost in parameter space. For the explicit form, the reader is referred to Eqs. (2.44)–(2.47) of Ref. [36].

The other alternative fit employed by Djukanovic *et al.* is the summation method [86–89]. This technique works by summing over the time dependence of the three-point correlation functions, which yields

$$\begin{aligned} R(t) &= \sum_{\tau=a}^{t-a} C^{3pt}(t, \tau) / \sqrt{C_{\mathbf{p}'}^{2pt}(t) C_{\mathbf{p}}^{2pt}(t)} \\ &\rightarrow \text{constant} + t \mathcal{J}_{11} + O(t e^{-\Delta E t}), \end{aligned} \quad (41)$$

where  $\Delta E$  is the gap in energies between the ground state and the first excited state. The ground state matrix element is then extracted by fitting the slope of  $R$  with respect to  $t$ . This benefits from increased suppression of excited states and reduced dependence on choice of fit parameters.

The summary of results used in this work are listed in Table II. The number of gauge ensembles used, and the size of the subset of those ensembles at physical masses, are listed in the third and fourth columns. For the number of ensembles, higher counts typically lead to better control of systematics.

The three separate quark actions used in these results are listed in the fifth column of Table II. The results from RQCD and Djukanovic *et al.* share subsets of the same gauge ensembles from the Coordinated Lattice Simulation (CLS) effort [90], with nonperturbatively order  $a$ -improved Wilson clover fermions [91, 92], and generate their own correlation functions on those ensembles. Sharing gauge ensembles leads to correlations in the results which are unknown and will need to be addressed in this

work. Though the NME result employs the same fermion action as RQCD and Djukanovic *et al.*, the gauge ensembles used by NME are generated independently and are uncorrelated. The result from PNDME also uses a Wilson clover action for the “valence” quarks (those quarks that are explicitly included in the correlation function constructions), these correlation functions are computed on gauge ensembles that were generated with a Highly-Improved Staggered Quark (HISQ) action [93–95] for the quarks in the “sea” (virtual quark-antiquark loops). These results are therefore also uncorrelated with the other Wilson clover results. Lastly, the ETM result uses the twisted mass action [96–98], which is also uncorrelated with the others.

The fit methods, which were outlined in this section, are enumerated in the sixth column of Table II. In broad terms, the three methods used for fitting the correlation functions to extract energies and matrix elements are the “Bayesian prior exponential” method, which involves fitting to the forms in Eq. (37) directly with priored coefficients, or the  $\chi$ PT-inspired and summation (Eq. (41)) method techniques employed by RQCD and Djukanovic *et al.*, respectively.

The last column of Table II gives the parameterizations from the LQCD results that were used in this work. The employed parameterizations are all  $z$  expansion. The order of the expansions are listed, with the  $z$  expansion either being carried up to  $k_{\max} = 2$  (labeled as  $z^2$ ) or  $k_{\max} = 3$  ( $z^3$ ). For all of the  $z$  expansion parameterizations, no sum rules were used. Since  $g_A$  is an output of LQCD computations, no constraint fixing the intercept was employed either.

#### IV. FIT RESULTS

This section delves into the results of fitting to the LQCD form factors. Sec. IV A explores the fits to form factor derivatives outlined in Sec. II B 1. Sec. IV B likewise goes into detail about sampled form factors outlined in Sec. II B 2. Several systematic variations are employed to test the sensitivity to various choices. Secs. IV A and IV B deal with systematics that are specific to each of the fit methods, respectively. Sec. IV C deals with systematics that are common to both methods.

Throughout this section, the plotted form factors are normalized by the deuterium result in Ref. [45] to improve the visibility of the curves. Uncertainties using the derivatives fit method of Sec. IV A are inflated by the derating factor  $\beta^{\text{cov}}$  according to Eq. (19) to account for unknown correlations between LQCD results. Unlike the sister paper [50], no regularization term is used for the  $z$  expansion coefficients in this work, instead relying on the residuals to constrain the form factor values. No exceptionally large parameter values are observed in any of the fit results.

##### A. Fits to Derivatives

In this subsection, the fits employing analytic derivatives of the form factors to construct residuals are explored. The philosophy behind choosing this fit method is that the form factor should be insensitive to higher-order  $z$  expansion coefficients, where empirically the slope and intercept are enough to constrain the form factor. If the fits are optimized over the central value and first derivative of the form factor at only a single value of  $Q^2$ , the form factor shape is still described well over a reasonably large range of  $Q^2$ . Adding evaluations at more  $Q^2$  points does not provide much additional constraint on the shape beyond what is obtained from linear behavior with  $z$ .

In the present work, the  $Q^2$  behavior of the form factor is expected to be described well over the range 0–1 GeV $^2$ , governed by the range of  $Q^2$  that is probed by LQCD computations. This range can be extended if LQCD computations are carried out for  $Q^2$  values larger than 1 GeV $^2$ .

Much of the behavior in the range 1–2 GeV $^2$  in this work is controlled by the sum rules in Eq. (4). Without imposing these sum rules, there is no expectation that the form factor should be well behaved at all. Although it is more theoretically justified to forgo sum rules to avoid potentially adding bias, including the sum rules is a practical consideration for experimental applications in Monte Carlo event generators where it is necessary to statistically sample the form factor out to large  $Q^2$ . The figures in the remainder of the work are plotted out to 2 GeV $^2$  so that the extrapolation of the form factor beyond the expected 1 GeV $^2$  cutoff can be examined qualitatively. The effect of removing the sum rules is also explored in more detail in Sec. IV C 1.

The resulting fit quality for all of the fits to derivatives that appear in this subsection are listed in Table III. The first column gives the description of the fits involved. These descriptions include at least the  $k_{\max}$  and the highest order of derivatives used as residuals (either 1st derivatives or 2nd derivatives). Where appropriate, alternative values of  $Q^2_{\min}$  and  $Q^2_{\text{compare}}$ , as defined in Eq. (42), or  $Q^2_{\text{anchor}}$ , the  $Q^2$  value for an included anchor point, are also listed.

The naive  $\chi^2$ , computed assuming all unknown correlations are set to 0, and DoF are listed for each fit in Table III. In addition, the derating factors from Sec. II C 1 and the corresponding  $p$  values are given. The value  $p^{\text{derated}}$  can be treated as an upper bound on the  $p$  value given the variations in the covariance matrix. If  $p^{\text{derated}}$  is less than 0.05, this can be used as evidence to exclude those fit assumptions. However, neither  $p$  value represents a lower bound: even if both  $p$  values are greater than 0.05, this does not guarantee that the corresponding fit model is consistent with the chosen LQCD inputs. The last two columns give the first two fit parameters that are optimized in the fits. In the case of  $z$  expansion fits, the  $a_1$  coefficient and  $a_2$  coefficient (when  $k_{\max} > 5$  or no sum rules are used) are reported. The dipole fit

Collaboration	Ref.	$N_{\text{ens}}$	$N_{\text{ens}}^{\text{phys}}$	quark action	fit method	parameterization
RQCD 2020	[36]	37	2	clover	$\chi^2$ PT-inspired	$z^2$ , no sum rules
NME 2022	[76]	7	0	clover	Bayesian prior exponential	$z^2$ , no sum rules
Djukanovic <i>et al.</i> 2022	[79]	14	1	clover	summation	$z^2$ , no sum rules
PNDME 2023	[81]	13	2	clover (on HISQ)	Bayesian prior exponential	$z^2$ , no sum rules
ETM 2023	[80]	3	3	twisted mass	Bayesian prior exponential	$z^3$ , no sum rules

TABLE II. Comparison of the relevant details of the LQCD results used in this work. The first and second columns give the name of the collaboration and the reference for the work. The third and fourth columns respectively denote the total number of ensembles and the number of ensembles at physical pion mass for each work. The quark action is given in the fifth column. The PNDME result uses a different quark action for the valence (Wilson clover) and sea quarks (Highly-Improved Staggered Quarks (HISQ)). The fit method used to extract excited states and axial matrix elements is given in the sixth column. Finally, the parameterization reported as a final result in each reference is given in the last column.

lists the value for  $M_A$  that is obtained from the fit.

### 1. Included Derivatives

The fits explored in this subsection test the sensitivity to where the form factor values and derivatives are evaluated. This includes the number of evaluation points, at what  $Q^2$  values they are probed, and what quantities are probed at each point.

The nominal choice of where to evaluate the form factors and derivatives is at the value  $Q^2 = -t_0$ , using the  $t_0$  defined for each individual LQCD result. This is the expansion point for the fit  $z$  expansion parameterization and the most natural place to evaluate derivatives for that parameterization, as discussed in Sec. II B 1. In cases where  $t_0 = 0$ , the comparison point is moved slightly away from  $Q^2 = 0$ . The default point where evaluations for each LQCD result are done is summarized by the value

$$Q_{\text{compare}}^2 = \max[Q_{\text{min}}^2, |-t_0|], \quad (42)$$

with  $Q_{\text{min}}^2 = 0.05 \text{ GeV}^2$  as the nominal choice. Other choices for  $Q_{\text{min}}^2$  will be explored in Sec. IV A 2.

The nominal fit takes only the central value and first derivative of the form factor for each LQCD result, although the process generalizes to higher-order derivatives. This provides 2 residuals per LQCD result, both the central value and derivative evaluated at  $Q_{\text{compare}}^2$ . The parameterizations have at least 3  $z$  expansion coefficients though, so there is still some freedom to select other residuals to fit against. The most natural option is to include second-order derivatives at the same evaluation point. Another option is to add an anchor point, the form factor central value evaluated at some higher  $Q^2$  point.

A comparison of fits to first derivatives only with different choices of  $k_{\text{max}}$  is shown in Fig. 1. The nominal fit with  $k_{\text{max}} = 6$  is shown against  $k_{\text{max}} = 5$  and  $k_{\text{max}} = 7$  fits. The  $k_{\text{max}} = 5$  result shows indications of being overfit, with a poor goodness-of-fit and lower  $p$  values.

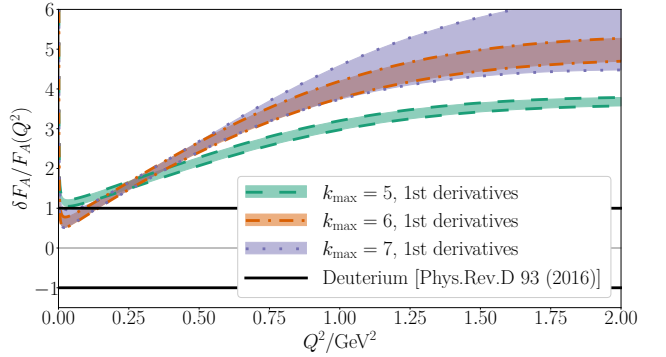


FIG. 1. Plot of the axial form factor fits from this work normalized by the  $z$  expansion deuterium result from Ref. [45]. The uncertainty band for the fit with  $k_{\text{max}} = 5$  and up to first-order derivatives only is given by the teal shaded region bordered by dashed lines. A similar fit with  $k_{\text{max}} = 6$  ( $k_{\text{max}} = 7$ ) is shown as the orange band with a dot-dashed border (blue-violet band with a dotted border). For reference, the normalized range  $0 \pm 1$  of the  $z$  expansion result is shown as black lines.

The  $k_{\text{max}} = 5$  fit also disagrees with the  $k_{\text{max}} = 6$  fit across the majority of the  $Q^2$  range. The reported value of  $p^{\text{derated}}$  for  $k_{\text{max}} = 5$  is just below the threshold such that this fit ansatz can be ruled out. The  $k_{\text{max}} = 7$  fit has a similar goodness-of-fit and  $p$  values to the  $k_{\text{max}} = 6$  fit, but a larger uncertainty at high  $Q^2$ . The decrease of  $\chi^2$  resulting from increasing  $k_{\text{max}}$  to 7 does not appreciably improve the  $p$  value, suggesting that the additional parameter only acts to inflate the uncertainties without providing a substantially better description of the input data. Since the  $k_{\text{max}} = 7$  fit includes only up to first-order derivatives, the only reason there is any constraint on the  $a_3$  coefficient is because the  $Q_{\text{compare}}^2$  is offset to  $Q_{\text{min}}^2$  for the parameterizations expanded at  $t_0 = 0$ . The fit residuals are still mainly dominated by the contributions from the coefficients  $a_1$  and  $a_2$ , so the constraint on  $a_3$  is not substantial. This is reflected in the fit posterior  $a_3 \approx 1.06(97)$ , with effectively 100% uncertainty.

A comparison of fits with up to second derivatives for

Description	$\chi^2$	$\nu$	$\beta^{\text{Gof}}$	$\beta^{\text{cov}}$	$p^{\text{naive}}$	$p^{\text{derated}}$	$a_1$	$a_2$
$k_{\max} = 5$ , 1st derivatives	21.11	9	1.19	1.21	0.01	0.04	-1.901( 8)	—
$k_{\max} = 6$ , 1st derivatives (nominal)	7.14	8	1.20	1.18	0.52	0.65	-1.701( 42)	0.26( 9)
$k_{\max} = 7$ , 1st derivatives	7.00	7	1.19	1.16	0.43	0.55	-1.658( 95)	0.43(35)
$k_{\max} = 6$ , 2nd derivatives	25.35	13	1.17	1.21	0.02	0.06	-1.638( 11)	0.02( 5)
$k_{\max} = 7$ , 2nd derivatives	13.73	12	1.00	1.16	0.32	0.32	-1.741( 25)	-0.05( 5)
$k_{\max} = 8$ , 2nd derivatives	10.13	11	1.14	1.12	0.52	0.63	-1.563( 74)	0.94(39)
$k_{\max} = 6$ , 1st derivatives, $Q_{\text{compare}}^2 = 0.25 \text{ GeV}^2$	12.11	8	1.24	1.18	0.15	0.28	-1.535( 37)	0.07( 7)
$k_{\max} = 6$ , 1st derivatives, $Q_{\text{compare}}^2 = 0.50 \text{ GeV}^2$	12.55	8	1.23	1.22	0.13	0.25	-1.646( 44)	0.18( 9)
$k_{\max} = 6$ , 1st derivatives, $Q_{\min}^2 = 0.00 \text{ GeV}^2$	5.50	8	1.05	1.05	0.70	0.73	-1.687( 30)	0.29( 8)
$k_{\max} = 6$ , 1st derivatives, $Q_{\min}^2 = 0.10 \text{ GeV}^2$	11.05	8	1.23	1.19	0.20	0.34	-1.660( 51)	0.15( 9)
$k_{\max} = 7$ , 1st derivatives, $Q_{\text{anchor}}^2 = 0.10 \text{ GeV}^2$	15.63	12	1.17	1.13	0.21	0.35	-1.777( 29)	-0.14( 5)
$k_{\max} = 7$ , 1st derivatives, $Q_{\text{anchor}}^2 = 0.75 \text{ GeV}^2$	20.82	12	1.28	1.10	0.05	0.17	-1.734( 27)	-0.20(15)
$k_{\max} = 7$ , 1st derivatives, $Q_{\text{anchor}}^2 = 1.00 \text{ GeV}^2$	21.60	12	1.01	1.12	0.04	0.05	-1.756( 30)	-0.21(16)
$k_{\max} = 2$ , 1st derivatives, no sum rules	8.16	8	1.23	1.18	0.42	0.58	-1.726( 77)	-0.27(20)
$k_{\max} = 3$ , 1st derivatives, no sum rules	6.76	7	1.20	1.16	0.45	0.58	-1.620(102)	0.87(76)
$k_{\max} = 6$ , 1st derivatives, $t_0 = -0.25 \text{ GeV}^2$	7.51	8	1.19	1.18	0.48	0.61	-1.771( 36)*	0.35( 8)*
Description	$\chi^2$	$\nu$	$\beta^{\text{Gof}}$	$\beta^{\text{cov}}$	$p^{\text{naive}}$	$p^{\text{derated}}$	$M_A$	—
dipole, 1st derivatives	13.41	9	1.14	1.19	0.14	0.23	1.219( 15)	—

TABLE III. Summary of fit results for fits to derivatives, enumerated in the same order that they first appear in figures within this section. The first column gives a description of the fit that was computed. The naive  $\chi^2$ , assuming all of the unknown covariances are 0, is given in the second column. The third column, labeled  $\nu$ , gives the DoF for the fit. The fourth and fifth columns give the derating factors  $\beta^{\text{Gof}}$  and  $\beta^{\text{cov}}$ , respectively, as discussed in Sec. II C 1. The  $p$  value computed using the naive  $\chi^2$  is listed in the sixth column, and the derated  $p$  value accounting for all variations of the covariance matrix within a 99% confidence interval is given in the seventh column. The second-to-last column gives the  $z$  expansion coefficient multiplying the  $z^1$  term in the power series, which is the lowest-order fit parameter, or the value of  $M_A$  for the dipole fit. The last column gives the coefficient multiplying the  $z^2$  term for the  $z$  expansion fits. For the row labeled with a description “ $k_{\max} = 6$ , 1st derivatives,  $t_0 = -0.25 \text{ GeV}^2$ ,” marked with an asterisk, the printed  $z$  expansion coefficients  $a_1$  and  $a_2$  are the translated coefficients using the prescription set out in Sec. II B 3. The raw  $z$  expansion coefficient values obtained for this fit are  $(a_1, a_2) = (-1.671(48), -0.68(9))$ .

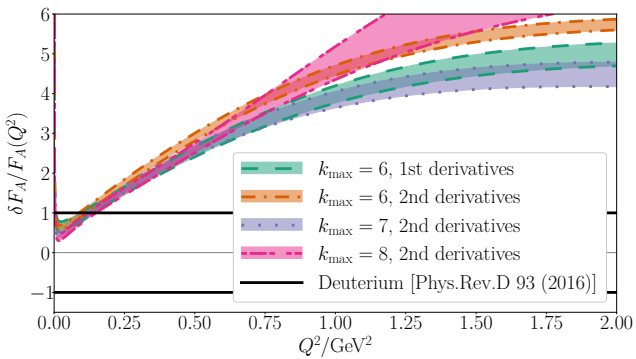


FIG. 2. Plot of the axial form factor fits from this work normalized by the  $z$  expansion deuterium result from Ref. [45]. The uncertainty band for the nominal result with  $k_{\max} = 6$  and up to first-order derivatives only is given by the teal shaded region bordered by dashed lines. Fits with up to second derivatives for  $k_{\max} = 6, 7$ , and 8 are shown as an orange band with a dot-dashed border, a blue-violet band with a dotted border, and a pink band with a triple-dash border, respectively. For reference, the normalized range  $0 \pm 1$  of the  $z$  expansion result is shown as black lines.

different choices of  $k_{\max}$  is shown in Fig. 2. This plot also shows the nominal fit,  $k_{\max} = 6$  with up to first derivatives, for reference. To account for the extra constraints

on the fit parameters,  $k_{\max}$  is chosen to be 1 larger than in Fig. 1. Like with the fits to first derivatives, the  $k_{\max} = 7$  fit to second derivatives is largely identical to the nominal fit in the range  $Q^2 \sim 0.1$ – $1.0 \text{ GeV}^2$ . For  $Q^2 \lesssim 0.1 \text{ GeV}^2$ , the fit is still compatible within  $2\sigma$ . The  $k_{\max} = 6$  fit to second derivatives departs from the nominal fit, accompanied by poor  $p$  values. The smallest  $k_{\max}$  ( $k_{\max} = 6$  here) again gives low  $p$  values that are small enough to be deemed incompatible, but the  $k_{\max} = 7$  and 8 fits have  $p$  values that are acceptable. The  $k_{\max} = 8$  fit has a compatible shape for  $Q^2 \lesssim 0.5 \text{ GeV}^2$ , but then increases to values considerably larger than the nominal fit.

Increasing to  $k_{\max} = 8$  yields a  $p$  value comparable to the nominal fit, suggesting that the additional degrees of freedom are meaningfully constrained by the fit parameters. These coefficients are again only probed by the residuals for the  $t_0 = 0$  results with  $Q_{\min}^2 \neq 0$ , as was the case for  $k_{\max} = 7$  fits with up to first derivatives in the discussion of Fig. 1. However, the parameters fixed by sum rule constraints in this fit take absolute values larger than 20. By contrast, the  $k_{\max} = 7$  fit with second derivatives has sum rule parameters up to absolute values of less than 6, and the nominal fit with  $k_{\max} = 6$  has parameter absolute values less than 2. If a regularization term was included in this fit, the regularization would add a significant penalty to the  $\chi^2$  for the  $k_{\max} = 8$  fit, spoiling the apparent compatibility of the fit. For this

reason, the  $k_{\max} = 8$  fit is not considered a good fit.

## 2. $Q^2$ Evaluation Points

Modifications of the specific values of  $Q^2$  where the residuals are evaluated are considered as another alternative method for evaluating sensitivity to systematics. Testing for compatibility between these different choices of included residuals gives confidence in the selection of a nominal fit. There are a number of selections of  $Q^2$  that are considered throughout the derivative fitting process:

1. the  $Q^2$  where the residuals for the primary evaluations are performed, labeled by  $Q^2_{\text{compare}}$ ;
2. the  $Q^2$  for primary evaluations that are expanded about 0, more specific than  $Q^2_{\text{compare}}$  and labeled by  $Q^2_{\min}$  in Eq. (42); and
3. the  $Q^2$  for any additional anchor points, labeled by  $Q^2_{\text{anchor}}$ .

These three possibilities will be tested in this subsection.

Fig. 3 shows the results of testing sensitivity to the value of  $Q^2_{\text{compare}}$ . Three choices all at  $k_{\max} = 6$  are utilized, either evaluating derivatives at the nominal choice defined in Eq. (42) or fixing all residuals to be evaluated at one choice of  $Q^2$ . The value  $Q^2_{\text{compare}} = 0.25 \text{ GeV}^2$  is chosen to approximate  $-t_0 = 0.28 \text{ GeV}^2$  used in Ref. [45], and  $-t_0 = 0.50 \text{ GeV}^2$  as the natural expansion point for the nominal fit in this work. While the fits employing Eq. (42) are constructed in a way to be dominated by only the lowest-order  $z$  expansion coefficients, as indicated in Eq. (11), the fits with fixed  $Q^2_{\text{compare}}$  produce a nonzero  $z$  and probe all of the  $z$  expansion coefficients at once.

Qualitatively, the fits in Fig. 3 appear largely consistent with each other, with some slight tensions at the  $2\text{-}3\sigma$  level between the nominal choice using Eq. (42) and the  $Q^2_{\text{compare}} = 0.25 \text{ GeV}^2$  expansion point. These tensions are mainly confined to  $Q^2$  below about  $0.2 \text{ GeV}^2$  and  $Q^2$  above around  $0.75 \text{ GeV}^2$ . The values of  $a_1$  obtained for this fit is in tension as well, with the  $Q^2_{\text{compare}} = 0.25 \text{ GeV}^2$  giving a  $3.0\sigma$  difference. In contrast, the  $Q^2_{\text{compare}} = 0.50 \text{ GeV}^2$  fit exhibits much better agreement across the board and only a  $0.9\sigma$  tension between values of  $a_1$ . The tensions appear to come from disagreements between the LQCD results on the slope at the new  $Q^2$  points. Although the tensions are present in both fits with fixed  $Q^2_{\text{compare}}$ , the residuals tend to pull equally in both directions for  $Q^2_{\text{compare}} = 0.50 \text{ GeV}^2$ , whereas the pull is biased toward smaller  $a_1$  in the  $Q^2_{\text{compare}} = 0.25 \text{ GeV}^2$  fit. The fixed expansion points come with mildly decreased goodness-of-fit, yielding  $p$  values less than 0.3, compared to the  $p^{\text{derated}}$  bound of 0.65 for the nominal fit. This suggests that the fixed expansion point is less favorable than the nominal choice, although not appreciably so.

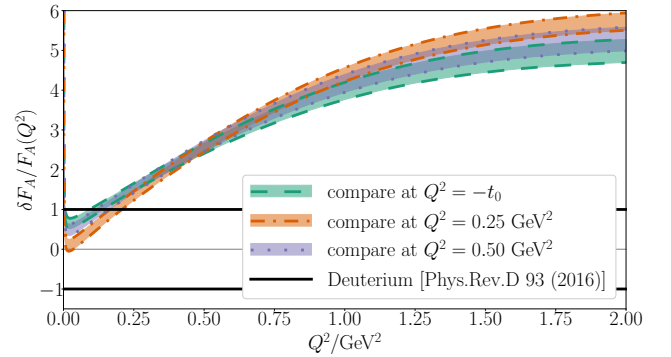


FIG. 3. Plot of the axial form factor fits from this work normalized by the  $z$  expansion deuterium result from Ref. [45]. The uncertainty band for the nominal result, evaluating the form factor and its derivatives for each separate LQCD result at its own value of  $Q^2 = -t_0$ , is given as the teal shaded region bordered by dashed lines. When  $t_0 = 0$ , the minimum value  $Q_0^2$  is used in place of  $t_0$ , as described in the text. Fits evaluating the form factor and its derivatives at  $Q^2 = 0.25 \text{ GeV}^2$  and  $0.50 \text{ GeV}^2$  are shown as the orange band with a dot-dashed border and the blue-violet band with a dotted border, respectively. For reference, the normalized range  $0 \pm 1$  of the  $z$  expansion result is shown as black lines.

Rather than evaluating all of the LQCD results to a single  $Q^2$ , a less disruptive choice is to only change the value of  $Q^2_{\min}$  used in Eq. (42). The nominal choice is  $Q^2_{\min} = 0.05 \text{ GeV}^2$ , but the other choices  $Q^2_{\min} = 0$  and  $Q^2_{\min} = 0.10 \text{ GeV}^2$  are also explored in Fig. 4.

Choosing  $Q^2_{\min} = 0$  is entirely consistent with the nominal choice, including a consistent value of  $a_1$ , smaller uncertainty, and even slightly better  $p$  values. However, this choice ignores the complication that arises from fixing the value of  $g_A$ , as mentioned in Sec. II B 1. For this reason, the ansatz with  $Q^2_{\min} = 0$  is not chosen as a nominal fit. The other choice at  $Q^2_{\min} = 0.10 \text{ GeV}^2$  is also consistent with the nominal choice, with less than a  $1\sigma$  shift in  $a_1$  and the form factor values across the entire plotted  $Q^2$  range. The  $p$  values are also lower than that of the nominal fit, but still at a reasonable level of  $p^{\text{derated}} \lesssim 0.4$ .

Fig. 5 shows the nominal  $k_{\max} = 6$  fit compared to  $k_{\max} = 7$  fits that include an anchor point at various values of  $Q^2_{\text{anchor}}$ . The choices  $Q^2_{\text{anchor}} = 0.10 \text{ GeV}^2$ , which sits between the  $Q^2 = -t_0$  evaluation points, as well as  $0.75$  and  $1.00 \text{ GeV}^2$  beyond the largest value of  $t_0$  are shown for comparison. All of the choices yield similar fits across the range  $Q^2 \sim 0.1\text{--}1.25 \text{ GeV}^2$  when compared to each other and the nominal fit. Only mild tensions  $\lesssim 1.5\sigma$  are observed for  $a_1$  across the fits. The  $p$  values are reduced when including an anchor point, mostly due to growing tensions at larger values of  $Q^2$ , and only the fit with  $Q^2_{\text{anchor}} = 1.00 \text{ GeV}^2$  has a  $p$  value low enough to be deemed unacceptable.

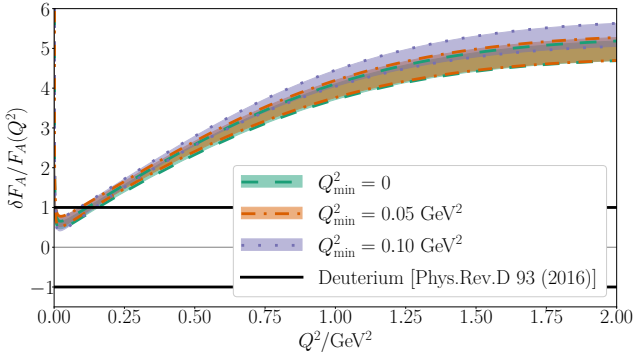


FIG. 4. Plot of the axial form factor fits from this work normalized by the  $z$  expansion deuterium result from Ref. [45]. The teal dashed, orange dot-dashed, and blue-violet dotted regions correspond to setting the minimum  $Q^2$  evaluation point, denoted by  $Q^2_{\min}$ , equal to 0, 0.05  $\text{GeV}^2$ , and 0.10  $\text{GeV}^2$ , respectively. This value is used for evaluation of the form factors and derivatives for results that set  $t_0 = 0$  (ETM and Djukanovic *et al.*). The nominal fit corresponds to the choice 0.05  $\text{GeV}^2$ , given by the orange dot-dashed region. For reference, the normalized range  $0 \pm 1$  of the  $z$  expansion result is shown as black lines.

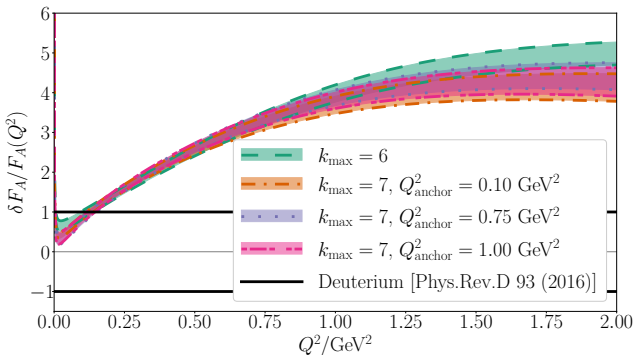


FIG. 5. Plot of the axial form factor fits from this work normalized by the  $z$  expansion deuterium result from Ref. [45]. The teal dashed region corresponds to the nominal fit with no anchor point. The orange dot-dashed, blue-violet dotted, and pink triple-dashed ranges, which all lie on top of each other, correspond to  $k_{\max} = 7$  fits with an anchor point at  $Q^2_{\text{anchor}} = 0.10, 0.75$ , and  $1.00 \text{ GeV}^2$ , respectively. For reference, the normalized range  $0 \pm 1$  of the  $z$  expansion result is shown as black lines.

## B. Fits to Sampled Form Factors

Fits to the form factor over a range of equidistant  $Q^2$  values are also considered as a more conventional alternative to fitting derivatives in the previous subsection. Like with the derivatives fits, form factors in this subsection are fit with sum rules and presented as ratios to the deuterium fit of Ref. [45].

These sampled fits are described in Sec. II B 2. A covariance matrix is assembled over the parameters from each of the LQCD results that has been modified ac-

cording to the Schmelling procedure in Sec. II C 2. One thousand randomly sampled sets of parameters are produced respecting the known covariances. These parameters are used to compute form factor central values for  $Q^2$  in the range  $\{0.0, 0.1, \dots, 1.0\} \text{ GeV}^2$  for each LQCD result. Residuals and an uncorrelated  $\chi^2$  loss function with a fixed set of errors are constructed according to Eq. (13). Additional fits were performed testing with 4 times the random samples and 4 times smaller spacing between  $Q^2$  values, both producing negligible difference compared to the nominal choice.

Unlike the derivatives fits, a proper goodness-of-fit cannot be assessed for these sampled form factor fits. The goodness-of-fit can be made to produce a  $p$  value arbitrarily close to 1 by fitting a denser set of  $Q^2$ . However, comparisons of reduced  $\chi^2$  values for a given fixed set of  $Q^2$  can still be performed to assess the relative fit quality of similar sampled fits.

Joint fits with the sampled form factor and other data cannot be easily performed either, for example fitting the LQCD results together with other neutrino scattering data. Like with the  $p$  values, choosing a denser set of  $Q^2$  would correspondingly increase the number of residuals in an overall  $\chi^2$ . The fit results could be arbitrarily skewed toward the LQCD by adding more  $Q^2$  evaluation points. This is a primary reason to favor the derivatives fits to the form factor, since the weight of the LQCD in the overall fit is more limited.

### 1. Schmelling Factor Variation

Fits with different Schmelling scale factors  $f$  are depicted in Fig. 6. One striking observation is that the uncertainty band for the fully correlated ( $f = 1$ ) fit is significantly larger than the uncertainty band of the nominal fit with the derivatives method. These two methods handle the unknown covariances quite differently from each other. The derivatives method makes use of the derating procedure, which more directly quantifies the amount of uncertainty inflation by exploring the full space of available correlated variations, allowing for variations where different offdiagonal elements take different relative sizes. The form factor sampling method used here applies the Schmelling procedure, which scales all of the unknown covariances with the same factor  $f$ .

The three values  $f = 1, 0.5$ , and  $0$ , all fit with  $k_{\max} = 6$ , are shown together. The scale  $f$  is only applied to the statistical uncertainty of the LQCD parameters that have unknown cross-correlations. These three fits have drastically different uncertainties, where  $f = 0$  (with unknown correlations set to exactly 0) corresponds to a form factor uncertainty about 50% the size of the fully-correlated ( $f = 1$ ) result at  $Q^2 = 0.5 \text{ GeV}^2$  and 30% at  $Q^2 = 1.0 \text{ GeV}^2$ .

Given the relative size of the uncertainties of the form factor method versus the derivatives method, the uncorrelated ( $f = 0$ ) case will be adopted as default for the

remaining form factor method variations. Note that a larger Schmeling factor will only inflate the uncertainties without changing the central value, so compatibility between fits will only get better as  $f$  increases. The direct comparison between the two fit methods with the uncorrelated and fully-correlated fits be revisited in Sec. IV C.

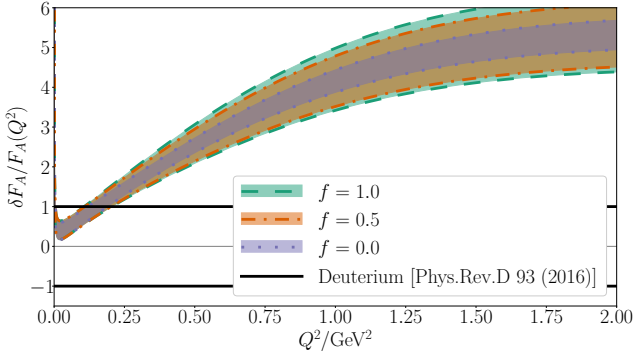


FIG. 6. Plot of the axial form factor fits from this work normalized by the  $z$  expansion deuterium result from Ref. [45]. All fits shown here have  $k_{\max} = 6$ . The teal dashed, orange dot-dashed, and blue-violet dotted regions correspond to the fits with the offdiagonal scale factor for the Schmeling procedure (defined in Eq. (22)) set to  $f = 1, 0.5$ , and  $0$ , respectively. For reference, the normalized range  $0 \pm 1$  of the  $z$  expansion result is shown as black lines.

## 2. $k_{\max}$ Variation

The plot of variations of the fit form factor over increasing  $k_{\max}$  is shown in Fig. 7. The corresponding reduced  $\chi^2$  values for the  $k_{\max} = 5, 6$ , and  $7$  fits are  $1.49, 0.82$ , and  $0.83$ , respectively. Like for the derivatives fit, the  $k_{\max} = 5$  result is likely overfit and departs from other fit results at low and intermediate  $Q^2$ . Increasing to  $k_{\max} = 7$  does not significantly improve over  $k_{\max} = 6$ , yielding a larger uncertainty at high  $Q^2$  and a slightly larger reduced  $\chi^2$ . The fit parameter values for the  $k_{\max} = 6$  fit are (taking  $a_3$  from the sum rules)

$$(a_1, a_2, a_3) = \left( -1.627(63), 0.18(12), 1.11(37) \right), \quad (43)$$

compared to the fit parameters for the  $k_{\max} = 7$  fit,

$$(a_1, a_2, a_3) = \left( -1.648(73), -0.06(28), 1.52(65) \right). \quad (44)$$

The fit parameters for these fits are unsurprisingly consistent with each other.

## C. Comparisons Between Methods

Having explored a number of form factor systematics for both averaging methods to decide on the nominal fit

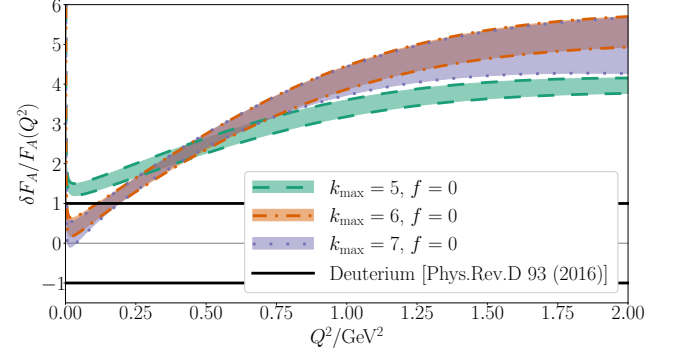


FIG. 7. Plot of the axial form factor fits from this work normalized by the  $z$  expansion deuterium result from Ref. [45]. The teal dashed, orange dot-dashed, and blue-violet dotted regions correspond to the fits with  $k_{\max} = 5, 6$ , and  $7$ , respectively. For reference, the normalized range  $0 \pm 1$  of the  $z$  expansion result is shown as black lines.

choices, the results of the averaging schemes can now be compared to each other. The method of fitting derivatives will be taken as the nominal choice for the final fit result, with the sampled form factor fit used as a validation. There are a number of reasons to prefer the derivatives fit over the sampled form factor:

1. the residuals for the derivatives fit can be defined analytically rather than stochastically;
2. fitting to derivatives has a natural choice for selecting the  $Q^2$  to compare against, specifically at  $Q^2 = -t_0$ ;
3. when number of residuals is less than the rank of the covariance matrix, the transformation from the set of input set of  $z$  expansion parameters to the residuals preserves the invertibility of the covariance matrix without additional modifications.

The analytic form of the derivatives method makes it simpler to form a combined fit with other sources, such as with experimental neutrino scattering data.

The comparison of the nominal choices for each fit method are shown in Fig. 8. The fit to form factor derivatives is more precise than the sampled form factor fits even for the uncorrelated ( $f = 0$ ) form factor sampling method. The relative size of the (correlated) derivatives fit with derating and the (uncorrelated) sampled fit might lead to the assumption that the LQCD results are closer to uncorrelated than fully correlated. However, correlations are not the only factor at play in the overall precision of the fits. The differences between the assumptions of the two fits, namely only examining the central values versus also examining the first derivatives, can change the overall precision of the fit. It is likely that both details play a role in the final fit precision.

The derivatives fit stays within the  $1\sigma$  band of the uncorrelated sampled fit over nearly the entire  $Q^2$  range,

only departing for  $Q^2 \lesssim 0.1 \text{ GeV}^2$ . This trend is also seen in Fig. 5, where the different choices of  $Q^2$  anchor point drag the form factor below the nominal fit at low  $Q^2$ . This could be a consequence of slight tensions between the parameterizations preferred from fitting the central values versus the first derivatives. Adding the anchor points gives twice as many central values informing the fits as derivatives, which will bias the fit in favor of the central values of the LQCD curves. Likewise, the sampled form factor fit includes no derivatives at all. Since the fits with anchor points produces less favorable  $p$  values than the nominal fit, and because the nominal fit also has larger uncertainties in the  $Q^2 \lesssim 0.1 \text{ GeV}^2$  range where the tension is seen, this slight difference is ignored.

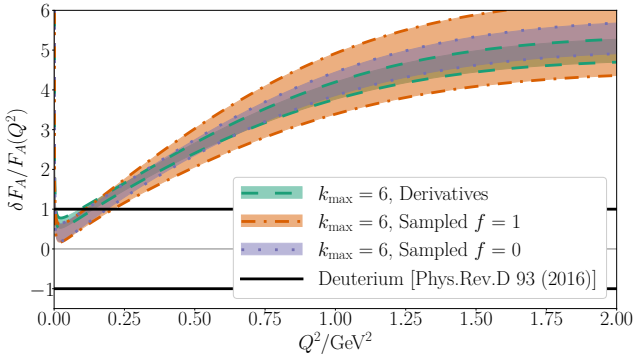


FIG. 8. Plot of the axial form factor fits from this work normalized by the  $z$  expansion deuterium result from Ref. [45]. The teal dashed region corresponds to the nominal fit for the derivatives fit method. The orange dot-dashed region and the blue-violet dotted region correspond to sampled form factor fits, either with the assumption of unknown correlations being fully-correlated ( $f = 1$ ) or uncorrelated ( $f = 0$ ), respectively. For reference, the normalized range  $0 \pm 1$  of the  $z$  expansion result is shown as black lines.

### 1. Removing Sum Rules

Fig. 9 shows the effects of dropping the sum rule constraints regulating the large  $Q^2$  behavior from the fits. The sampled form factor fits both take  $f = 0$  for uncorrelated results. The fits all use 2 free parameters, giving  $k_{\max} = 6$  for fits with 4 sum rules or  $k_{\max} = 2$  for fits without sum rules. The constraint fixing the value  $F_A(Q^2 = 0) = g_A$  is still imposed for all fits.

The fits both with and without sum rules agree well up to  $Q^2 \sim 0.75 \text{ GeV}^2$ . At this point, the derivative fit with no sum rules starts to diverge from the full set of fits. The sampled form factor fits with no sum rules start to diverge above  $Q^2 \sim 1.0 \text{ GeV}^2$ . This is a reflection of the range of constraints on the form factor: for the derivatives fit, the largest  $Q^2$  where the form factor is constrained comes from the NME result with  $-t_0 = 0.5 \text{ GeV}^2$ ; the sampled form factor fit has a  $Q^2$  range extending up to  $1.0 \text{ GeV}^2$ .

Beyond these values, the form factor coefficients are not effectively constrained. Without the sum rules to regulate the form factor, the form factor shape is free to exhibit divergent behavior. However, in the range where fit constraints exist, the form factor should be described at least as well as without the sum rules provided  $k_{\max}$  is large enough to obtain a reasonable fit.

The sum rules do not introduce a large bias into the  $z$  expansion coefficients. For the derivatives method, the fit coefficients with sum rules are

$$(a_1, a_2) = (-1.701(42), 0.26(9)), \quad (45)$$

and without sum rules are

$$(a_1, a_2) = (-1.726(77), -0.27(20)). \quad (46)$$

For the sampled form factors, the fit with sum rules gives

$$(a_1, a_2) = (-1.630(63), 0.18(13)), \quad (47)$$

and without sum rules

$$(a_1, a_2) = (-1.623(65), 0.02(21)). \quad (48)$$

This gives less than a  $1\sigma$  shift in the value of  $a_1$ , but a more significant shift of  $2.5\sigma$  for  $a_2$  between the derivative method fits with and without sum rules.

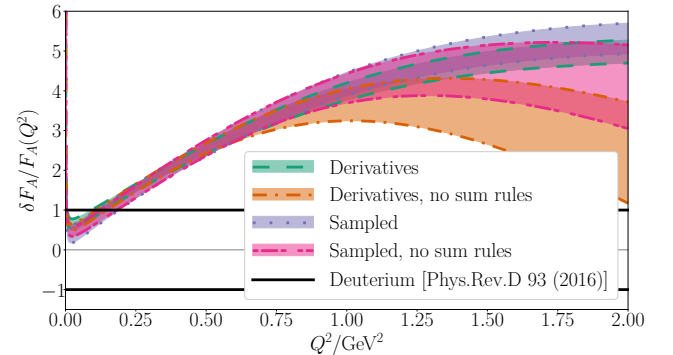


FIG. 9. Plot of the axial form factor fits from this work normalized by the  $z$  expansion deuterium result from Ref. [45]. The teal dashed and orange dot-dashed regions correspond to fits with the derivatives method, while the blue-violet dotted and pink triple-dashed regions correspond to the sampled form factor fits. The teal dashed region and blue-violet dotted regions include the full set of four sum rules, and the orange dot-dashed and pink triple-dashed regions do not include any sum rule constraints. For reference, the normalized range  $0 \pm 1$  of the  $z$  expansion result is shown as black lines.

### 2. $t_0$ Variation

The zero point in the definition of  $z$ , denoted by  $t_0$ , is another fixed parameter that should not make a significant difference in the fit. These variations are explored

in Fig. 10, where fits to the nominal  $t_0 = -0.50 \text{ GeV}^2$  and a variation  $t_0 = -0.25 \text{ GeV}^2$  are plotted.

The value  $t_0 = -0.50 \text{ GeV}^2$  is selected to match onto a value optimized for the MINER $\nu$ A results in Ref. [50]. However, the range of  $Q^2$  probed by LQCD calculations only extends up to  $Q^2 \sim 1 \text{ GeV}^2$ . The larger magnitude  $t_0$  means that  $|z| \lesssim 0.34$  over the range  $0 \leq Q^2 < 1 \text{ GeV}^2$ , versus for  $|z| \lesssim 0.25$  for  $t_0 = -0.25 \text{ GeV}^2$ . This means that the form factor could potentially converge with fewer parameters if the smaller magnitude of  $t_0$  was selected.

No substantial deviations are seen in the entire  $Q^2$  range. This is supported by the extracted  $z$  expansion coefficients as well. The nominal fit with  $t_0 = -0.50 \text{ GeV}^2$  yields the values

$$(a_1, a_2) = (-1.701(42), 0.26(9)). \quad (49)$$

To compare to this, the translated  $z$  expansion coefficients, defined by the prescription in Sec. II B 3, for the modified value  $t_0 = -0.25 \text{ GeV}^2$  are

$$(a_1, a_2) = (-1.771(36), 0.35(8)), \quad (50)$$

which agree to the level of  $1.3\sigma$  for  $a_1$  and  $1\sigma$  for  $a_2$ . For the sampled form factors, the fit with  $t_0 = -0.50 \text{ GeV}^2$  gives

$$(a_1, a_2) = (-1.630(63), 0.18(13)), \quad (51)$$

and the fit for  $t_0 = -0.25 \text{ GeV}^2$  gives the translated values

$$(a_1, a_2) = (-1.678(59), 0.22(12)), \quad (52)$$

which correspond again only to  $1\sigma$  shifts.

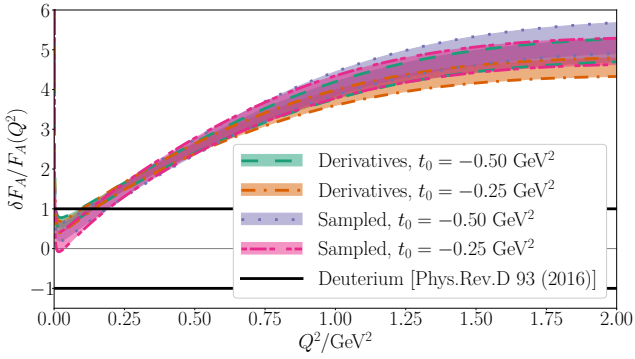


FIG. 10. Plot of the axial form factor fits from this work normalized by the  $z$  expansion deuterium result from Ref. [45]. The teal dashed and blue-violet dotted regions show the fits to  $t_0 = -0.50 \text{ GeV}^2$  with the derivatives and sampled form factor fit methods, respectively. The orange dot-dashed and pink triple-dashed regions correspond to fits with  $t_0 = -0.25 \text{ GeV}^2$  for the derivatives and sampled methods, respectively. For reference, the normalized range  $0 \pm 1$  of the  $z$  expansion result is shown as black lines.

### 3. Fits to Dipole Form

The LQCD results are fit to a dipole form factor parameterization and compared to the nominal fits in Fig. 11. The nominal fits for both the derivatives and sampled form factor methods are shown as the teal dashed and orange dot-dashed regions, respectively. Superimposed is the fit to the dipole form factor, computed using the sampled form factor method.

The sampled form factor fit to the dipole parameterization yields an axial mass  $M_A = 1.236(38) \text{ GeV}$ . The enhanced  $M_A$  is typical of form factors with a slow  $Q^2$  falloff, as is seen in the LQCD results. The dipole form factors depicted in Fig. 11 exhibit deviations from the  $z$  expansion form factors, predicting a larger form factor for  $Q^2 \lesssim 0.5 \text{ GeV}^2$  and smaller for  $Q^2 \gtrsim 1.0 \text{ GeV}^2$ . The reduced  $\chi^2$  for the fit also does not perform as well as the  $z$  expansion, with a value of  $\chi^2/\nu \approx 1.24$  versus the  $z$  expansion value  $\chi^2/\nu \approx 0.82$ .

This figure demonstrates how the dipole parameterization fails to capture the form factor shape, even with an enhanced axial mass parameter. The slow falloff of the form factor with  $Q^2$  is captured at the expense of a systematic bias in the form factor shape, first overpredicting the  $z$  expansion form factor at low  $Q^2$  then underpredicting relative to the  $z$  expansion at high  $Q^2$ . The dipole parameterization does not have enough parametric freedom to change this trend, only to modify the value of  $Q^2$  where the crossover occurs.

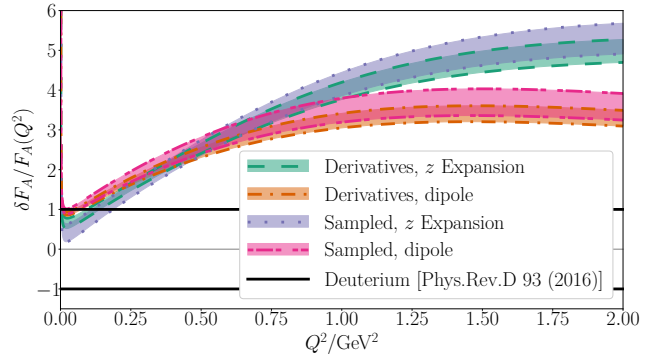


FIG. 11. Plot of the axial form factor fits from this work normalized by the  $z$  expansion deuterium result from Ref. [45]. The teal dashed and blue-violet dotted regions show the fits to a  $z$  expansion parameterization with the derivatives and sampled form factor fit methods, respectively. The orange dot-dashed and pink triple-dashed regions correspond to dipole fits using the derivatives and sampled methods, respectively. For reference, the normalized range  $0 \pm 1$  of the  $z$  expansion result is shown as black lines.

### D. Fit Parameterizations

In this subsection, final fits of the form factors are given. The values with two significant digits of uncer-

tainty are provided for quick comparisons between fits. In addition, the full set of parameter central values, including the parameters obtained from sum rule constraints, are provided along with the covariance matrix. These values are provided for posterity so that the form factors can be used elsewhere.

### 1. Fit to Derivatives

The nominal fit to derivatives of the form factor is reproduced here. The parameters fixed in the fits match those listed in Table I. The  $k_{\max} = 6$  fit is given by

$$(a_1, a_2) = (-1.701(42), 0.263(90)) \quad (53)$$

with the covariance matrix

$$\begin{pmatrix} 0.00175929 & -0.00294651 \\ -0.00294651 & 0.00807158 \end{pmatrix}. \quad (54)$$

With the sum rule constraints applied, the full set of coefficients are

$$\begin{aligned} & (a_0, \dots, a_6) \\ &= \begin{pmatrix} 0.72115656, & -1.70104640, & 0.26324902, \\ 1.53433681, & 0.01061114, & -1.49893610, \\ 0.67062898 \end{pmatrix}. \end{aligned} \quad (55)$$

The axial radius squared obtained from this parameterization is

$$r_A^2 = 0.369(30) \text{ fm}^2. \quad (56)$$

The unknown correlations between LQCD results prevent the assignment of a definitive  $p$  value. Instead, covariance derating [56] is used to estimate a 99% confidence interval upper bound on the goodness-of-fit. This limits  $p \lesssim p^{\text{derated}} \approx 0.65$ . Assuming the unknown correlations are identically 0, the  $p$  value can be computed directly as  $p^{\text{naive}} \approx 0.52$  from  $\chi^2 \approx 7.14$  and 8 degrees of freedom.

For a  $k_{\max} = 7$  fit with the same residuals as the  $k_{\max} = 6$  fit, the fit parameters are

$$(a_1, a_2, a_3) = (-1.658(95), 0.431(347), 1.06(97)) \quad (57)$$

with the covariance matrix

$$\begin{pmatrix} 0.00910412 & 0.02592048 & -0.08986544 \\ 0.02592048 & 0.12033231 & -0.30490195 \\ -0.08986544 & -0.30490195 & 0.93874891 \end{pmatrix}. \quad (58)$$

With the sum rule constraints applied, the full set of coefficients are

$$\begin{aligned} & (a_0, \dots, a_7) \\ &= \begin{pmatrix} 0.72240694, & -1.65806627, & 0.43099261, \\ 1.06243035, & -0.68256510, & 1.06363538, \\ -1.59271086, & 0.65387696 \end{pmatrix}. \end{aligned} \quad (59)$$

The axial radius squared obtained from this parameterization is

$$r_A^2 = 0.341(62) \text{ fm}^2. \quad (60)$$

For this fit, the  $p$  values are  $p^{\text{derated}} \approx 0.55$  and  $p^{\text{naive}} \approx 0.43$  from  $\chi^2 \approx 6.99$  and 7 degrees of freedom.

As an additional comparison point, the  $k_{\max} = 7$  fit with the second derivatives included is given by

$$(a_1, a_2, a_3) = (-1.741(25), -0.048(49), 2.13(19)) \quad (61)$$

with the covariance matrix

$$\begin{pmatrix} 0.00063056 & 0.00022664 & -0.00454614 \\ 0.00022664 & 0.00244803 & -0.00422261 \\ -0.00454614 & -0.00422261 & 0.03561104 \end{pmatrix}. \quad (62)$$

With the sum rule constraints applied, the full set of coefficients are

$$\begin{aligned} & (a_0, \dots, a_7) \\ &= \begin{pmatrix} 0.72415239, & -1.74051938, & -0.04845258, \\ 2.13430614, & 1.41235527, & -5.65778627, \\ 4.15759466, & -0.98165022 \end{pmatrix} \end{aligned} \quad (63)$$

The axial radius squared obtained from this parameterization is

$$r_A^2 = 0.423(16) \text{ fm}^2. \quad (64)$$

For this fit, the  $p$  values are exactly equal with  $p^{\text{naive}} = p^{\text{derated}} \approx 0.32$  from  $\chi^2 \approx 13.73$  and 12 degrees of freedom.

### 2. Fit to Sampled Form Factor

The nominal fit to derivatives of the form factor is reproduced here. The parameters fixed in the fits match those listed in Table I. The  $k_{\max} = 6$  fit is given by

$$(a_1, a_2) = (-1.630(63), 0.18(13)) \quad (65)$$

with the covariance matrix

$$\begin{pmatrix} 0.00390684 & -0.00480561 \\ -0.00480561 & 0.01588552 \end{pmatrix}. \quad (66)$$

With the sum rule constraints applied, the full set of coefficients are

$$\begin{aligned} & (a_0, \dots, a_6) \\ &= \begin{pmatrix} 0.72217245, & -1.62716067, & 0.17896964, \\ 1.11227915, & 1.02836466, & -2.30667668, \\ 0.89205145 \end{pmatrix} \end{aligned} \quad (67)$$

The axial radius squared obtained from this parameterization is

$$r_A^2 = 0.424(52) \text{ fm}^2. \quad (68)$$

For a  $k_{\max} = 7$  fit with the same residuals as the  $k_{\max} = 6$  fit, the fit parameters are

$$(a_1, a_2, a_3) = (-1.649(73), -0.06(27), 1.51(65)) \quad (69)$$

with the covariance matrix

$$\begin{pmatrix} 0.00526364 & 0.00659750 & -0.04317334 \\ 0.00659750 & 0.07403803 & -0.12297087 \\ -0.04317334 & -0.12297087 & 0.42623351 \end{pmatrix}. \quad (70)$$

With the sum rule constraints applied, the full set of coefficients are

$$(a_0, \dots, a_7) = (0.72415215, -1.64720287, -0.05571462, 1.49700975, 2.16783943, -5.42758266, 3.45633330, -0.71483448) \quad (71)$$

The axial radius squared obtained from this parameterization is

$$r_A^2 = 0.476(79) \text{ fm}^2. \quad (72)$$

### E. Comparison to LQCD Parameterizations

The fit result from Eqs. (53)–(55) is compared to the parameterizations it was fit to in Fig. 12. The LQCD calculations produce predictions of axial matrix elements at discrete, finite values of  $Q^2$  in the range 0–1 GeV $^2$ , where the upper end of the range is limited only by finite computation resources. These discrete values are fit across a range of lattice spacings, lattice volumes, and masses to produce the QCD predictions given here. The LQCD form factors are most precisely constrained at low-to-moderate  $Q^2$ , with the expectation that systematics will be largest at  $Q^2$  close to 0. The diverging form factor uncertainty for the LQCD fits at  $Q^2 = 0$  is a consequence of the exact constraint  $F_A(Q^2 = 0) = g_A^\beta$  imposed on the deuterium result from Ref. [45].

The averaged form factor agrees well with the individual LQCD results across the range of  $Q^2$  shown in the figure. None of the fit parameterizations include sum rules, so the agreement between the results is expected to degrade above the 1 GeV $^2$  cutoff. Despite this expectation, the averaged form factor continues to follow along with all of the results except RQCD above the 1 GeV $^2$  cutoff, at least in part due to the growing uncertainties at large  $Q^2$ . In particular, the averaged form factor follows closely with the NME result, which is the most precise of the available parameterizations.

The form factor uncertainty is improved significantly after the average. Part of this constraint, especially at low  $Q^2$  originates from the sum rule enforcing the condition  $F_A(Q^2 = 0) = g_A^\beta$ , which gives an infinitely precise prediction at  $Q^2 = 0$ . However, the form factor is also about a factor of 2 more precise than the LQCD results individually, which would be expected for an average of 5

uncorrelated results with similar uncertainties. The precision of the form factor is about 1.2% for  $Q^2 = 0.5$  GeV $^2$  and 2.2% at  $Q^2 = 1.0$  GeV $^2$ . This is near the limit of the precision that can be achieved without considering systematic corrections due to isospin-breaking effects, which are expected to enter at around the percent level [77].

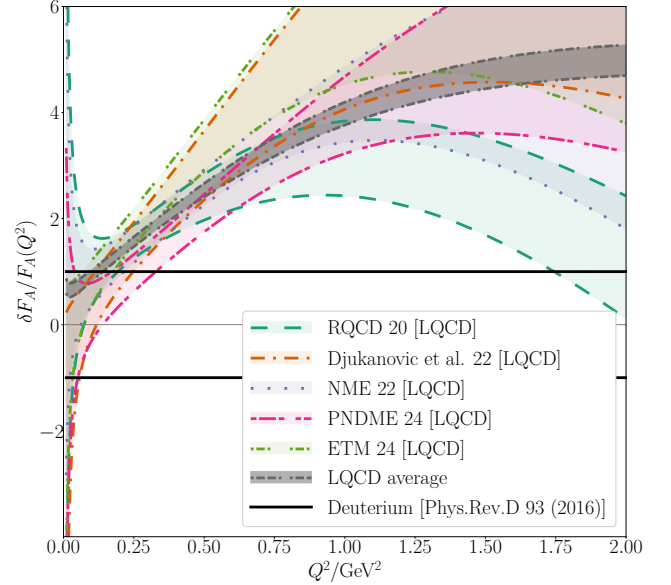


FIG. 12. Plot of the axial form factor results from the references in Table II normalized by the  $z$  expansion deuterium result from Ref. [45]. The fit result from Eqs. (53)–(55) is shown as the gray region bounded by dot-dash-dot lines. For reference, the normalized range  $0 \pm 1$  of the  $z$  expansion result is shown as black lines.

### F. Comparison to Neutrino Scattering Data

The comparison between the LQCD average, neutrino-deuterium, and antineutrino-proton scattering data are shown in Fig. 13. The result from Ref. [45] is shown for reference. The fit to the deuterium bubble chamber data has implemented a different selection criterion for selecting the optimal amount of regularization for the  $z$  expansion parameters, appealing to an L-curve regularization scheme [99, 100] versus arguments from unitarity. This results in an approximate degeneracy between the floating normalizations on the deuterium cross section and the form factor shape, which leads to a large systematic uncertainty expressed as a dependence on the low- $Q^2$  cut. The envelope of form factor shapes out to  $1\sigma$  that are explored by different choices of  $Q^2$  cut are given by the blue-violet region bounded by dotted lines. With the increased uncertainty from the fit envelope due to systematic uncertainty, the deuterium does constrain the form factor shape strongly enough to compete with

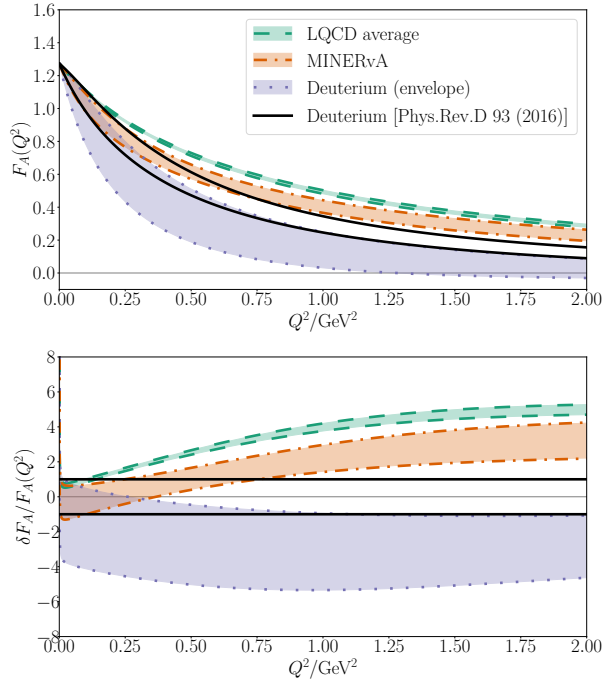


FIG. 13. The top panel shows the final choices for the axial form factor parameterizations taken from Ref. [50]. The bottom panel shows those same parameterizations normalized to the deuterium result of Ref. [45]. The LQCD Average fit (green dashed region) is taken from Eq. (53). The curve labeled MINER $\nu$ A (orange dot-dashed) is obtained from fitting the  $z$  expansion to antineutrino-proton scattering data in Refs. [22, 23]. The curve labeled “Deuterium (envelope)” (blue-violet dotted) is taken from an envelope bounding two different kinematic cuts of fits to neutrino-deuterium bubble chamber scattering data [6–14]. For comparison, the result using neutrino-deuterium scattering data from Ref. [45] is plotted as an unfilled region bounded by black solid lines. The bottom panel shows the same curves, but normalized by the result from Ref. [45].

the MINER $\nu$ A or LQCD results.

A fit to the MINER $\nu$ A antineutrino-proton dataset using the same set of  $z$  expansion parameters as the LQCD is shown as the orange dot-dashed region. Like the LQCD, the MINER $\nu$ A fit exhibits a slower falloff with  $Q^2$  relative to the deuterium form factor. There is still a slight tension, at the level of about  $2\sigma$ , between the MINER $\nu$ A and LQCD. A combined fit between the two sources yields a fit that is dominated by the LQCD, lying almost entirely on top of the LQCD curve. This fit has been omitted from the figure. A  $p$  value test with a 1 DoF  $\Delta\chi^2$  comparison demonstrates that the two form factor constraints are consistent despite the slight tension, yielding  $\Delta\chi^2 \approx 3.2$  for a  $p$  value of 0.08. For a more comprehensive discussion of the connections to neutrino scattering data, the reader is referred to the sister paper, Ref. [50].

## V. DISCUSSION

Precise and accurate neutrino-nuclear cross sections are a necessity for next-generation neutrino oscillation experiments. The nuclear models needed to predict these cross sections are constructed from neutrino-nucleon amplitudes. These amplitudes are difficult to quantify from experiment alone. As an example, charged-current neutrino-nucleon quasielastic scattering requires high-statistics measurements and detection of events with neutrons produced in the final state. Given the relative importance of this low-energy interaction mechanism, it begs the question whether theory can be used to improve constraints on poorly-understood nucleon-level amplitudes. Of particular interest is the nucleon axial form factor, which dominates the uncertainty budget for neutrino-nucleon quasielastic scattering.

LQCD is a highly attractive candidate for providing theoretical inputs to neutrino-nuclear cross section predictions. Calculations performed with LQCD confer a number of advantages, such as rigorous uncertainty quantification and systematically improvable uncertainties. Recent LQCD calculations of the nucleon isovector axial form factor now pass key internal consistency checks, and also provide a consensus on the behavior of the form factor with respect to the momentum transfer dependence. This behavior is in conflict with fits to neutrino-deuterium scattering results but consistent with antineutrino-hydrogen scattering, suggesting that remnant nuclear effects may still be at play even in deuterium scattering measurements.

LQCD results also provide precise determinations of the form factor, leading to the appealing possibility of averaging the results to obtain an averaged LQCD isovector axial form factor more precise than the individual results. This possibility is explored in this work. Two strategies for averaging the results are employed to perform the averages: first, an averaging strategy that fits to derivatives of the form factor with respect to  $Q^2$ ; and second, a strategy that stochastically samples the form factor values over a set of equidistant  $Q^2$  evaluation points. Both strategies are compared to each other and average fits are produced.

The fit to the derivatives of the form factor takes advantage of the properties of the  $z$  expansion parameterization. Defined as a power series of a small expansion parameter  $z$ , the  $z$  expansion naturally suppresses the effects of higher-order powers of  $z$ . This leads to a form factor that can be approximately described by a linear function in  $z$  over some range of  $Q^2$ , which suggests that the form factor shape can be reasonably well described by its central value and derivatives at a single point. The ideal expansion point for this comparison is the value of  $t_0$ , which determines the value of  $Q^2$  at which  $z = 0$ . This strategy for averaging works remarkably well and gives a result consistent with the typical strategy of fitting to the stochastically-sampled form factors in the average, as seen in Fig. 8. This strategy can be defined

in completely analytically with a fixed number of residuals, adding to the appeal and lending more direct assessments of goodness-of-fit and compatibility with experimental datasets. The latter possibility is explored in a sister paper, Ref. [50].

The method of fitting to the derivatives has some drawbacks that must be considered. Fits to the derivatives are sensitive to the  $Q^2$  evaluation points that are used, particularly in constructing a fit with an invertible covariance matrix. The form factor cannot be taken to arbitrarily large  $k_{\max}$ , limited instead by the number of derivatives that are included and the spread of  $Q^2$  evaluation points that are used. If the evaluations are carried out only at the natural expansion point, i.e. evaluating the derivatives at  $Q^2 = -t_0$ , then this strategy is also sensitive to the variety of  $t_0$  values provided by the included results. Consistency is expected within the range of  $Q^2$  explored by the  $t_0$  values, but beyond that range the form factor can drift away from the desired central value. This is most apparent in Fig. 9, where the form factor drift in  $Q^2$  can be plainly seen when the sum rules are not there to regulate the large  $Q^2$  behavior. This can be somewhat alleviated by including anchor points or sum rules, but in this work the former case also gives poor goodness-of-fit as reported in Table II.

The derivatives method also permits more sophisticated ways to estimate the uncertainty inflation needed to account for unknown sources of correlation. The LQCD results can be subject to unknown correlations over their statistical uncertainties due to reuse of gauge configurations. In this work, the method of covariance derating introduced in Sec. II C 1 was used in the derivatives fitting method to assess the needed uncertainty inflation. The derating method reports only a modest increase in uncertainty when allowing for covariance fluctuations with a 99% confidence band, yielding a similar shape and precision as the sampled form factor with the assumption of no correlation between results as seen in Fig. 8. This is a believable conclusion given that the results do not share their statistical samples, only (subsets of) the gauge configurations on which those statistical samples are generated. With covariance derating, more guidance is provided on how to assign unknown correlations, allowing for a smaller uncertainty inflation when such an inflation is not needed.

The dipole parameterization shape visually disagrees with the results obtained from the  $z$  expansion fits, as seen in Fig. 11. Although the slower falloff with  $Q^2$  does result in an enhanced  $M_A$  (giving  $M_A \approx 1.21(2)$  GeV in Table III), the dipole form factor is still larger than the  $z$  expansion below  $Q^2 \lesssim 0.25$  GeV $^2$  and then smaller than the  $z$  expansion above  $Q^2 \gtrsim 0.75$  GeV $^2$ . This falls below several of the LQCD results for  $Q^2 \gtrsim 1.00$  GeV $^2$ . Even still, the derivatives fit in Table II yields a  $p$  value that is acceptable according to the criteria used to judge the  $z$  expansion parameterizations.

With the averaging strategy put forth in this work, the LQCD results can be fit together with the MINER $\nu$ A antineutrino-hydrogen scattering data. These fits produce a result that is nearly degenerate with the LQCD result in isolation. The fits from LQCD and MINER $\nu$ A are compatible with each other, as determined from a  $p$  value obtained from a  $\Delta\chi^2$  test with 1 DoF. The LQCD and MINER $\nu$ A, both independently and together, disagree with the results from neutrino-deuterium scattering, suggesting an uncontrolled systematic in the deuterium scattering data. These comparisons are explored in more detail in the sister paper to this work, Ref. [50]. With these considerations in mind, the recommendation is to opt for the LQCD results relying on the confidence gained from comparisons between LQCD and MINER $\nu$ A results.

## VI. ACKNOWLEDGMENTS

I would like to thank Sara Collins, Peter Denton, Rajan Gupta, Andreas Kronfeld, Kevin McFarland, Sungwoo Park, Sasha Tomalak, André Walker-Loud, Callum Wilkinson, and Clarence Wret, for useful discussions. Special thanks goes out to Lukas Koch for providing guidance for many of the details in Sec. II C 1 and additional functionality in the `nustattools` [57] package for the practical implementation of this work.

This work was performed under the auspices of the U.S. Department of Energy by Lawrence Livermore National Laboratory under Contract DE-AC52-07NA27344 and the Neutrino Theory Network Program under Grant DE-AC02-07CHI11359 and U.S. Department of Energy Award DE-SC0020250.

---

[1] Z. Djurcic *et al.* (JUNO), [arXiv:1508.07166 \[physics.ins-det\]](https://arxiv.org/abs/1508.07166) (2015), (unpublished).  
[2] R. Acciarri *et al.* (DUNE), [arXiv:1512.06148 \[physics.ins-det\]](https://arxiv.org/abs/1512.06148) (2015), (unpublished).  
[3] K. Abe *et al.* (Hyper-Kamiokande), [arXiv:1805.04163 \[physics.ins-det\]](https://arxiv.org/abs/1805.04163) (2018), (unpublished).  
[4] D. S. Ayres *et al.* (NO $\nu$ A) (2007), (unpublished).  
[5] B. Abi *et al.* (DUNE), [arXiv:2002.03005 \[hep-ex\]](https://arxiv.org/abs/2002.03005) (2020), (unpublished).  
[6] W. A. Mann *et al.*, *Phys. Rev. Lett.* **31**, 844 (1973).  
[7] S. J. Barish *et al.*, *Phys. Rev. D* **16**, 3103 (1977).  
[8] S. J. Barish *et al.*, *Phys. Rev. D* **19**, 2521 (1979).  
[9] K. L. Miller *et al.*, *Phys. Rev. D* **26**, 537 (1982).  
[10] N. J. Baker, A. M. Cnops, P. L. Connolly, S. A. Kahn, H. G. Kirk, M. J. Murtagh, R. B. Palmer, N. P. Samios, and M. Tanaka, *Phys. Rev. D* **23**, 2499 (1981).  
[11] T. Kitagaki *et al.*, *Phys. Rev. D* **28**, 436 (1983).  
[12] H. Wachsmuth, Neutrino and Muon Fluxes in the CERN 400-gev Proton Beam Dump Experiments (1979).

[13] S. J. M. Barlag, Quasi-elastic interactions and one-pion production by neutrinos and anti-neutrinos on a deuterium target (1984).

[14] D. Allasia *et al.*, *Nucl. Phys. B* **343**, 285 (1990).

[15] M. Hilt, B. C. Lehnhart, S. Scherer, and L. Tiator, *Phys. Rev. C* **88**, 055207 (2013), arXiv:1309.3385 [nucl-th].

[16] A. Liesenfeld *et al.* (A1), *Phys. Lett. B* **468**, 20 (1999), arXiv:nucl-ex/9911003.

[17] K. I. Blomqvist *et al.*, *Z. Phys. A* **353**, 415 (1996).

[18] A. Czarnecki, W. J. Marciano, and A. Sirlin, *Phys. Rev. Lett.* **99**, 032003 (2007), arXiv:0704.3968 [hep-ph].

[19] V. A. Andreev *et al.* (MuCap), *Phys. Rev. Lett.* **110**, 012504 (2013), arXiv:1210.6545 [nucl-ex].

[20] V. A. Andreev *et al.* (MuCap), *Phys. Rev. C* **91**, 055502 (2015), arXiv:1502.00913 [nucl-ex].

[21] R. J. Hill, P. Kammel, W. J. Marciano, and A. Sirlin, *Rept. Prog. Phys.* **81**, 096301 (2018), arXiv:1708.08462 [hep-ph].

[22] L. Zazueta *et al.* (MINERvA), *Phys. Rev. D* **107**, 012001 (2023), arXiv:2209.05540 [hep-ex].

[23] T. Cai *et al.* (MINERvA), *Nature* **614**, 48 (2023).

[24] S. Navas *et al.* (Particle Data Group), *Phys. Rev. D* **110**, 030001 (2024).

[25] A. S. Kronfeld, D. G. Richards, W. Detmold, R. Gupta, H.-W. Lin, K.-F. Liu, A. S. Meyer, R. Sufian, and S. Syritsyn (USQCD), *Eur. Phys. J. A* **55**, 196 (2019), arXiv:1904.09931 [hep-lat].

[26] B. C. Tiburzi, *Phys. Rev. D* **91**, 094510 (2015), arXiv:1503.06329 [hep-lat].

[27] B. C. Tiburzi, *PoS CD15*, 087 (2016), arXiv:1508.00163 [hep-lat].

[28] O. Bar, *Int. J. Mod. Phys. A* **32**, 1730011 (2017), arXiv:1705.02806 [hep-lat].

[29] O. Bar, *EPJ Web Conf.* **175**, 01007 (2018), arXiv:1708.00380 [hep-lat].

[30] O. Bär, *PoS LATTICE2018*, 061 (2018), arXiv:1808.08738 [hep-lat].

[31] O. Bar, *Phys. Rev. D* **99**, 054506 (2019), arXiv:1812.09191 [hep-lat].

[32] G. S. Bali, S. Collins, M. Gruber, A. Schäfer, P. Wein, and T. Wurm, *Phys. Lett. B* **789**, 666 (2019), arXiv:1810.05569 [hep-lat].

[33] Y.-C. Jang, R. Gupta, B. Yoon, and T. Bhattacharya, *Phys. Rev. Lett.* **124**, 072002 (2020), arXiv:1905.06470 [hep-lat].

[34] O. Bar, *Phys. Rev. D* **100**, 054507 (2019), arXiv:1906.03652 [hep-lat].

[35] O. Bär, *PoS LATTICE2019*, 078 (2019), arXiv:1907.03284 [hep-lat].

[36] G. S. Bali, L. Barca, S. Collins, M. Gruber, M. Löffler, A. Schäfer, W. Söldner, P. Wein, S. Weishäupl, and T. Wurm (RQCD), *JHEP* **05**, 126, arXiv:1911.13150 [hep-lat].

[37] C. C. Chang *et al.*, *Nature* **558**, 91 (2018), arXiv:1805.12130 [hep-lat].

[38] G. S. Bali, S. Collins, S. Heybrock, M. Löffler, R. Rödl, W. Söldner, and S. Weishäupl (RQCD), *Phys. Rev. D* **108**, 034512 (2023), arXiv:2305.04717 [hep-lat].

[39] R. Gupta, *Universe* **10**, 135 (2024), arXiv:2401.16614 [hep-lat].

[40] D. Djukanovic, G. von Hippel, H. B. Meyer, K. Ott�ad, and H. Wittig, *Phys. Rev. D* **109**, 074507 (2024), arXiv:2402.03024 [hep-lat].

[41] C. Alexandrou, S. Bacchio, J. Finkenrath, C. Iona, G. Koutsou, Y. Li, and G. Spanoudes, *Phys. Rev. D* **111**, 054505 (2025), arXiv:2412.01535 [hep-lat].

[42] Z. B. Hall *et al.*, (2025), arXiv:2503.09891 [hep-lat].

[43] R. Gupta, Y.-C. Jang, H.-W. Lin, B. Yoon, and T. Bhattacharya, *Phys. Rev. D* **96**, 114503 (2017), arXiv:1705.06834 [hep-lat].

[44] L. A. Russo *et al.*, *J. Phys. G* **52**, 043001 (2025), arXiv:2203.09030 [hep-ph].

[45] A. S. Meyer, M. Betancourt, R. Gran, and R. J. Hill, *Phys. Rev. D* **93**, 113015 (2016), arXiv:1603.03048 [hep-ph].

[46] A. S. Meyer, A. Walker-Loud, and C. Wilkinson, *Ann. Rev. Nucl. Part. Sci.* **72**, 205 (2022), arXiv:2201.01839 [hep-lat].

[47] O. Tomalak, R. Gupta, and T. Bhattacharya, *Phys. Rev. D* **108**, 074514 (2023), arXiv:2307.14920 [hep-lat].

[48] P. Abratenko *et al.* (MicroBooNE), *Phys. Rev. D* **105**, 072001 (2022), arXiv:2110.14028 [hep-ex].

[49] J. Tena-Vidal *et al.* (GENIE), *Phys. Rev. D* **106**, 112001 (2022), arXiv:2206.11050 [hep-ph].

[50] A. S. Meyer *et al.* (MINERvA), (2025), arXiv:2512.14097 [hep-ex].

[51] C. H. Llewellyn Smith, *Phys. Rept.* **3**, 261 (1972).

[52] G. P. Lepage and S. J. Brodsky, *Phys. Rev. D* **22**, 2157 (1980).

[53] R. J. Hill and G. Paz, *Phys. Rev. D* **82**, 113005 (2010), arXiv:1008.4619 [hep-ph].

[54] B. Bhattacharya, R. J. Hill, and G. Paz, *Phys. Rev. D* **84**, 073006 (2011), arXiv:1108.0423 [hep-ph].

[55] Y. Aoki *et al.* (Flavour Lattice Averaging Group (FLAG)), (2024), arXiv:2411.04268 [hep-lat].

[56] L. Koch, *Phys. Rev. D* **111**, 033002 (2025), arXiv:2410.22333 [stat.ME].

[57] L. Koch, Zenodo.10.5281/zenodo.1743358 (2025).

[58] M. Schmelling, *Phys. Scripta* **51**, 676 (1995).

[59] A. S. Meyer, R. J. Hill, A. S. Kronfeld, R. Li, and J. N. Simone, *PoS LATTICE2016*, 179 (2016), arXiv:1610.04593 [hep-lat].

[60] N. Hasan, J. Green, S. Meinel, M. Engelhardt, S. Krieg, J. Negele, A. Pochinsky, and S. Syritsyn, *Phys. Rev. D* **97**, 034504 (2018), arXiv:1711.11385 [hep-lat].

[61] K. I. Ishikawa, N. Ishizuka, Y. Kuramashi, Y. Nakamura, Y. Namekawa, Y. Taniguchi, N. Ukita, T. Yamazaki, and T. Yoshie (PACS), *Phys. Rev. D* **99**, 014504 (2019), arXiv:1807.06237 [hep-lat].

[62] E. Shintani, K.-I. Ishikawa, Y. Kuramashi, S. Sasaki, and T. Yamazaki, *Phys. Rev. D* **99**, 014510 (2019), [Erratum: *Phys. Rev. D* 102, 019902 (2020)], arXiv:1811.07292 [hep-lat].

[63] Y. Lin, A. S. Meyer, S. Gottlieb, C. Hughes, A. S. Kronfeld, J. N. Simone, and A. Strelchenko, *Phys. Rev. D* **103**, 054510 (2021), arXiv:2010.10455 [hep-lat].

[64] J. He *et al.*, *Phys. Rev. C* **105**, 065203 (2022), arXiv:2104.05226 [hep-lat].

[65] K.-I. Ishikawa, Y. Kuramashi, S. Sasaki, E. Shintani, and T. Yamazaki (PACS), *Phys. Rev. D* **104**, 074514 (2021), arXiv:2107.07085 [hep-lat].

[66] A. S. Meyer *et al.*, *PoS LATTICE2021*, 081 (2022), arXiv:2111.06333 [hep-lat].

[67] S. Ohta (UKQCD), *PoS LATTICE2021*, 529 (2022), arXiv:2111.12972 [hep-lat].

[68] L. Barca, G. Bali, and S. Collins, *Phys. Rev. D* **107**, L051505 (2023), arXiv:2211.12278 [hep-lat].

[69] S. Ohta (LHP, RBC, UKQCD), *PoS LATTICE2022*,

116 (2023), arXiv:2211.16018 [hep-lat].

[70] J. Koponen, D. Djukanovic, G. von Hippel, H. B. Meyer, K. Ottnad, T. Schulz, and H. Wittig, PoS **LATTICE2022**, 113 (2023).

[71] S. Ohta, PoS **LATTICE2023**, 325 (2024), arXiv:2311.05894 [hep-lat].

[72] A. Hackl and C. Lehner, (2024), arXiv:2412.17442 [hep-lat].

[73] Y. Aoki, K.-I. Ishikawa, Y. Kuramashi, S. Sasaki, K. Sato, E. Shintani, R. Tsuji, H. Watanabe, and T. Yamazaki (PACS), Phys. Rev. D **112**, 074510 (2025), arXiv:2505.06854 [hep-lat].

[74] R. Tsuji, Y. Aoki, K.-I. Ishikawa, Y. Kuramashi, S. Sasaki, K. Sato, E. Shintani, H. Watanabe, and T. Yamazaki (PACS), (2025), arXiv:2505.10998 [hep-lat].

[75] A. Barone, D. Djukanovic, G. von Hippel, J. Koponen, H. B. Meyer, K. Ottnad, and H. Wittig, PoS **LATTICE2024**, 334 (2025), arXiv:2502.06305 [hep-lat].

[76] S. Park, R. Gupta, B. Yoon, S. Mondal, T. Bhattacharya, Y.-C. Jang, B. Joó, and F. Winter (Nucleon Matrix Elements (NME)), Phys. Rev. D **105**, 054505 (2022), arXiv:2103.05599 [hep-lat].

[77] V. Cirigliano, J. de Vries, L. Hayen, E. Mereghetti, and A. Walker-Loud, Phys. Rev. Lett. **129**, 121801 (2022), arXiv:2202.10439 [nucl-th].

[78] S. Park, (2025), private communication.

[79] D. Djukanovic, G. von Hippel, J. Koponen, H. B. Meyer, K. Ottnad, T. Schulz, and H. Wittig, Phys. Rev. D **106**, 074503 (2022), arXiv:2207.03440 [hep-lat].

[80] C. Alexandrou, S. Bacchio, M. Constantinou, J. Finkenrath, R. Frezzotti, B. Kostrzewa, G. Koutsou, G. Spanoudes, and C. Urbach (Extended Twisted Mass), Phys. Rev. D **109**, 034503 (2024), arXiv:2309.05774 [hep-lat].

[81] Y.-C. Jang, R. Gupta, T. Bhattacharya, B. Yoon, and H.-W. Lin (Precision Neutron Decay Matrix Elements (PNDME)), Phys. Rev. D **109**, 014503 (2024), arXiv:2305.11330 [hep-lat].

[82] E. E. Jenkins and A. V. Manohar, Phys. Lett. B **255**, 558 (1991).

[83] E. E. Jenkins, Nucl. Phys. B **368**, 190 (1992).

[84] A. Walker-Loud *et al.*, Phys. Rev. D **79**, 054502 (2009), arXiv:0806.4549 [hep-lat].

[85] K. I. Ishikawa *et al.* (PACS-CS), Phys. Rev. D **80**, 054502 (2009), arXiv:0905.0962 [hep-lat].

[86] L. Maiani, G. Martinelli, M. L. Paciello, and B. Taglienti, Nucl. Phys. B **293**, 420 (1987).

[87] S. Gusken, Nucl. Phys. B Proc. Suppl. **17**, 361 (1990).

[88] S. J. Dong, J. F. Lagae, and K. F. Liu, Phys. Rev. Lett. **75**, 2096 (1995), arXiv:hep-ph/9502334.

[89] S. Capitani, B. Knippschild, M. Della Morte, and H. Wittig, PoS **LATTICE2010**, 147 (2010), arXiv:1011.1358 [hep-lat].

[90] M. Bruno *et al.*, JHEP **02**, 043, arXiv:1411.3982 [hep-lat].

[91] B. Sheikholeslami and R. Wohlert, Nucl. Phys. B **259**, 572 (1985).

[92] J. Bulava and S. Schaefer, Nucl. Phys. B **874**, 188 (2013), arXiv:1304.7093 [hep-lat].

[93] E. Follana, Q. Mason, C. Davies, K. Hornbostel, G. P. Lepage, J. Shigemitsu, H. Trottier, and K. Wong (HPQCD, UKQCD), Phys. Rev. D **75**, 054502 (2007), arXiv:hep-lat/0610092.

[94] Z. Hao, G. M. von Hippel, R. R. Horgan, Q. J. Mason, and H. D. Trottier, Phys. Rev. D **76**, 034507 (2007), arXiv:0705.4660 [hep-lat].

[95] A. Hart, G. M. von Hippel, and R. R. Horgan (HPQCD), Phys. Rev. D **79**, 074008 (2009), arXiv:0812.0503 [hep-lat].

[96] R. Frezzotti, P. A. Grassi, S. Sint, and P. Weisz (Alpha), JHEP **08**, 058, arXiv:hep-lat/0101001.

[97] R. Frezzotti and G. C. Rossi, JHEP **08**, 007, arXiv:hep-lat/0306014.

[98] M. Constantinou *et al.* (ETM), JHEP **08**, 068, arXiv:1004.1115 [hep-lat].

[99] P. C. Hansen, SIAM Review **34**, 561 (1992), <https://doi.org/10.1137/1034115>.

[100] P. C. Hansen, The l-curve and its use in the numerical treatment of inverse problems (WIT Press, 2001) pp. 119–142.